Electromagnetic Design Optimization of V-Shaped Magnet IPM Synchronous Machines

by

Buddhika De Silva Guruwatta Vidanalage

A Thesis submitted to the Faculty of Graduate Studies of

The University of Manitoba

in partial fulfillment of the requirements for the degree of

MASTER OF SCIENCE

Department of Electrical and Computer Engineering

University of Manitoba,

Winnipeg, Manitoba

January 2018

Abstract

This thesis presents an electromagnetic design optimization for the V-shaped magnet Interior Permanent Magnet Synchronous Machines (IPMSMs) and conducts a comparative study on the predicted operating characteristics of the optimally designed machines. A local optimizer (nonlinear Simplex), a global optimizer (Genetic Algorithm) and a newly developed algorithm for multimodal design optimization are separately introduced and used to determine the dimensions of each optimized machine based on three distinctive Objective Functions (OFs) to minimize (i) the weight, (ii) the electromagnetic losses, and (iii) the weighted combination of losses and weight considering mechanical, thermal, and magnetic constraints. Using the comparative study conducted in this thesis, the advantages and disadvantages of each designed machine obtained by different optimization techniques and OFs are discussed especially in terms of the operating characteristics not directly included in the defined OFs. This study enables one to have more degrees of freedom in selecting a final design among the presented optimized designs.

In order to verify theoretical predictions, a prototype of the optimized machine is fabricated, and the output power, losses, and efficiency of the built machine are assessed using experimental analysis. The close agreement between the simulation and experimental results for the optimized IPMSM design verifies the accuracy, reliability, and effectiveness of the optimization approach and simulation analysis.

Acknowledgements

It is with immense gratitude that I acknowledge the support and guidance of my supervisor, Prof. Shaahin Filizadeh for his encouragements and insightful supervision during every stage of this thesis. It would not have been possible to write this dissertation without his continual encouragement, priceless guidance, and constructive feedback.

I would like to especially thank Dr. Mohammad Sedigh Toulabi for his valuable time, effort, and essential guidance and knowledge during this research.

I would like to extend a special thank you to my examining committee members, Dr. Ian Jeffrey, Dr. Udaya Annakage, and Dr. Pooneh Maghoul for taking the time to review this thesis.

I would also like to thank the academic and technical staff in the Department of Electrical and Computer Engineering of the University of Manitoba, and specifically Mr. Erwin Dirks for his help and technical discussions during the test rig preparation step.

Dedication

To

My family for their genuine support.

Table of Contents

Chapter 3

Chapter 4
Design Optimization of IPMSMs using GA and Nonlinear Simplex Algorithms

Chapter 5
Multimodal Design Optimization and Experimental Analysis

Chapter 6
Contributions, Conclusions, and Recommendations for Future Work

List of Tables

List of Figures

List of Abbreviations

A_{sl}	Slot area	(m^2)
AC	Alternating current	
B_m	Air gap flux density	(T)
B_r	Remnant flux density	(T)
B_{sy}	Magnetic flux density in the stator yoke	(T)
B_{ts}	Flux density in the stator teeth	(T)
B_{THD}	Total harmonic distortion of the air-gap flux density waveform	
$(B.H)_{max}$	Energy density	(MGOe)
C_{ea}	Coil end arc (or end winding)	(m)
CPSR	Constant power speed range	
Cs	Conductor size area	(m^2)
CW	Concentrated winding	
2D-FEM	Two-dimensional finite element method	
3D-FEM	Three-dimensional finite element method	
D_{ag}	Inner stator diameter	(m)
D_o	Outer stator diameter	(m)
D_{rc}	Rotor diameter	(m)
DC	Direct current	
DW	Distributed winding	
E	Back-EMF (rms)	(V)
E_c	Electrical conductivity	(S/m)
E_l	Electric loading	(A/m)
EMF	Electromotive force	(V)

FEM	Finite element method	
Gas	Genetic Algorithms	
H	Vertical coil span	
H_c	Coercive force	
I	Current-rms	(A)
IPMSM	Interior permanent magnet synchronous machine	
i_d,	D-axis current	(A)
i_q	Q-axis current	(A)
J	Current density	(A/mm^2)
k_c	Carter factor	
k_f	Stack factor	
k_{w1}	Fundamental winding factor	
L	Stack length	(m)
L_d	D-axis inductance	(H)
L_q	Q-axis inductance	(H)
L_{isw}	Inner stator slot width	(m)
L_{osw}	Outer stator slot width	(m)
L_{sh}	Stator slot height	(m)
L_{so}	Slot opening	(m)
L_{sw}	Tooth tip thickness	(m)
L_{sy}	Stator yoke height	(m)
L_{tw}	Tooth width	(m)
l_{fe}	Length of the iron bridge	(m)
l_i	Air-gap around permanent magnet	(m)
MMF	Magneto-motive force	(AT)

MTPA	Maximum torque per ampere	
n_{rs}	Speed (revolutions per second)	(rps)
n_s	Turn per slot	
OFs	Objective functions	
P_{cu}	Copper loss	(W)
P_h	Number of phases	
P_{iron}	Iron loss	(W)
P_{loss}	Total loss	(W)
P_{mL}	Magnet length	(m)
P_{mw}	Magnet width	(m)
P_{out}	Output power	(W)
PM	Permanent magnet	
PMSM	Permanent magnet synchronous machines	
PWM	Pulse-width modulation	
PSO	Particle swarm optimization	
P	Pole pairs	
Q_s	Slot number	
R	Phase resistance	(Ω)
RSM	Response surface method	
r_{tol}	Fractional tolerance	
S	Apparent power	(VA)
S_{en}	Sensitivity	
S_r	Saliency ratio	
SM	(Separately excited) synchronous machine	
SPMSM	Surface mounted permanent magnet synchronous machines	

SUMT	Sequential unconstrained minimization technique	
SyRM	Synchronous reluctance machines	
T	Developed torque	(N.m)
T_c	Thermal conductivity	(W/m.K)
THD	Total harmonic distortion	
T_{ph}	Turn per phase	
V_{d}	D-axis voltage	(V)
V_{q}	Q-axis voltage	(V)
$Weight$	Motor weight	(kg)
W_{cu}	Copper weight	(kg)
w_{fe}	Thickness of iron bridge	(m)
w_{l}	Winding layer	
W_{magnet}	Magnet weight	(kg)
W_{rotor}	Rotor weight	(kg)
W_{stator}	Stator weight	(kg)
A	Half of the magnet pitch	(rad)
Λ	Weighting factor	
λ_{pm}	Permanent magnet flux linkage	(Wb.N)
μ_{r}	Relative permeability	
η_{Peak}	Maximum efficiency	(%)
Ξ	Saliency ratio	
P	Density	(kg/m^3)
ρ_{cu}	Copper density	(kg/m^3)
ρ_{Fe}	Iron density	(kg/m^3)
ρ_{PM}	Magnet density	(kg/m^3)

T	Electrical resistivity	(Ω.m)
τ_{Cu}	Copper resistivity	(Ω.m)
ω_e	Electrical frequency	(rad/s)

Chapter 1

Introduction

Contents

The primary intention of this chapter is to discuss the characteristics and behavior of Permanent Magnet Synchronous Machines (PMSMs) focusing mainly upon the V-shaped magnet Interior Permanent Magnet Synchronous Machines (IPMSMs). The performance characteristics of such machines can be enhanced by applying design optimization algorithms to determine their key parameters and dimensions. Winding structures of an electric machine has a significant effect on its performance. Detailed explanations regarding two winding structures of interest known as Distributed Winding (DW) and Concentrated Winding (CW) are provided. Additionally, simulation-based design approaches used to verify the quality of the designs and an introduction to the numerical techniques are also presented in this chapter.

1.1 General Background

Faraday's law of electromagnetic induction in 1831 and Maxwell's four equations (laws) later in the 19th century triggered the rapid exponential development in the area of electrical machines. Nowadays, electric machines are used in a wide range of applications from micro-motors used in medical industry (such as in intracardiac blood pumps) to large motors used for

ship propulsion [1-4]. Electrical machines are categorized into two main types: Alternating Current (AC) machines and Direct Current (DC) machines. AC machines are the most commonly used type in high-performance applications due to their superior efficiency and dynamic performance [5]. There are two main types of AC machines, namely asynchronous or induction machines and synchronous machines. Induction machines are the most common type of AC motors used in residential, commercial and agricultural applications due to their high reliability. In such applications, induction machines are mainly found in water pumps, air conditioners, boilers and compressors, etc. [6]. Synchronous machines offer guaranteed constant (synchronous) speed regardless of variations in the load, facilitate operation under a wide range of power factors with excitation current control, and offer additional advantages of high torque density, excellent field-weakening capability, to name a few [7, 8]. Synchronous machines are expensive compared to induction machines and are found commonly in applications such as timers, electromechanical robots, metering pumps, speed controllers and electric vehicles [6].

Synchronous machines are categorized into three main types: (1) separately excited synchronous machines, (2) Synchronous Reluctance Machines (SyRMs) and (3) Permanent Magnet Synchronous Machines (PMSMs). A categorization of the different types of synchronous machines are shown in Figure 1.1, where the main types of rotor geometries are the salient and non-salient pole designs. In salient pole machines, the effective length of the air gap through which the flux passes is nonuniform due to the saliency of its poles, while non-salient pole rotor machines have a uniform air gap. In both of these machines, a DC supply is required for their excitation, and it is realized through brushed/brushless arrangements. SyRMs use the saliency caused by the difference between the d- and q- axis inductances to generate the driving torque. The objective of these machines is to create maximum inductance difference between the direct and quadrature axes

by employing a minimum direct axis and a maximum quadrature axis reluctance. These machines typically contain either no magnets or a very small number of permanent magnets embedded in the rotor to assist in torque production [9]. On the other hand, there are two main types of PMSMs known as salient and non-salient machines according to the magnet arrangement on the rotor [10].

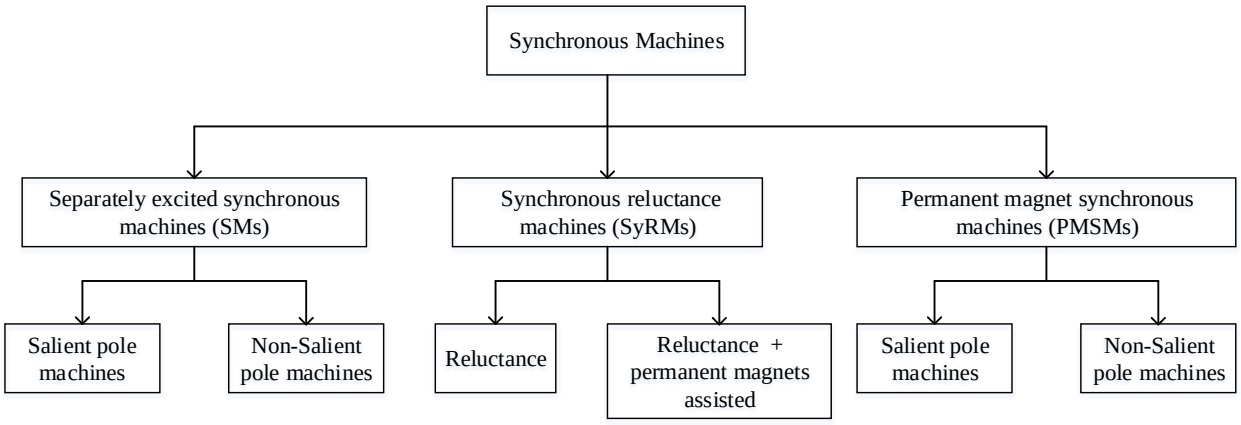

Figure 1.1 Types of synchronous machines [10].

1.1.1 Permanent Magnet Synchronous Machines (PMSMs)

Recent advancements in the field of high-energy PM materials and power electronics have increased the PM feasibility in various applications including electric machines. In PMSMs, PMs generate the required no load air-gap flux density by replacing the rotor copper windings and eliminating the required DC power. Hence, PMSMs offer high efficiency, simplify machine construction by eliminating slip rings, commutator, and carbon brushes, and offer better dynamic performance with relatively high air-gap flux density [11].

In recent decades, PMSMs have been extensively utilized in a wide range of applications including industrial applications (industrial robots), transportation (railway traction motors), and renewable energy systems (wind turbine PMSM generator). This is due to their high torque-density, reliability, high efficiency, and excellent flux-weakening capability [8, 12-15]. According to the magnet placement on the rotor, PMSMs are classified into two main categories: Surface

mounted PMSMs (SPMSMs) and Interior PMSMs (IPMSMs). The permanent magnets of the SPMSMs are mounted on their rotors and are buried in the rotors in IPMSMs as shown in Figure 1.2 and Figure 1.3. The focus of this thesis is on IPMSMs as they have three main advantages over SPMSMs [5, 16]:

a) Buried magnets give IPMSMs a structurally stronger rotor and make them more rigid in high-speed applications;

b) Salient pole structure offers additional useful reluctance torque, thus giving the motor greater field-weakening capability and higher torque density;

c) The possibility of changing the geometry of the buried magnets in the rotor of an IPMSM makes it possible to have a high flux concentration.

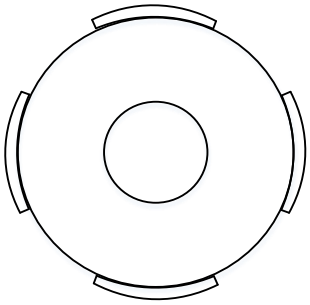

Figure 1.2 Rotor geometry of Surface mounted PMSM.

The characteristics of IPMSMs are determined by their rotor geometries. Four commonly used rotor topologies include: (i) spoke, (ii) tangential, (iii) V-shaped and (iv) U- shaped types. These different types are illustrated in Figure 1.2 [17].

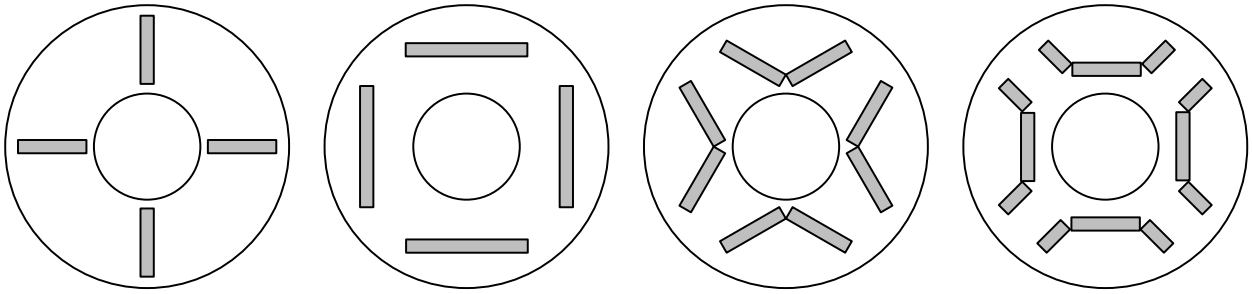

(a) (b) (c) (d)

Figure 1.3 Various IPMSM rotor geometries (a) spoke (b) tangential (c) V-shaped (d) U- shaped types.

The analysis in [17] verifies that the spoke type motor has the widest Constant Power Speed Range (CPSR). However, it is unable to meet the requirements of sufficient average torque, low torque ripple, large reluctance torque, etc. in the low-speed region due to its large flux leakage, low average torque, low power/volume ratio, low power factor, and poor efficiency. On the other hand, the tangential-type motor has the highest average torque, power/volume ratio, power factor, and lowest torque ripple and cogging torque. However, it has the shortest CPSR. V-shaped magnet IPMSMs have better overall performance in terms of the average torque, reluctance torque, power/volume ratio, and power factor.

The winding structure of an AC machine has a major impact on the machine's magneto-motive force (MMF) generation as well as on the machine's induced voltage when subjected to a rotating magnetic field. It also influences the inductance of the machine through the relative coupling between the windings. There are two main winding arrangements in a machine: concentrated winding (CW) and distributed winding (DW).

In the construction of a CW, the opposite-polarity end of the corresponding phase coil is located in the next slot; therefore, end windings do not overlap. This decreases the overall axial length of the machine, reduces copper losses, and simplifies manufacturing [18]. However, a CW arrangement has inherent disadvantages such as higher cogging torque, and reduced saliency and

overall developed torque. Furthermore, it has increased MMF harmonics, which result in significant increases in eddy current and hysteresis losses [18, 19]. However, Magnussen and Sadarangani [18] showed that by selecting an appropriate fractional-slot distribution, the winding factor and quality of the EMF waveform can be significantly increased, resulting in increased output torque. In addition, this fractional-slot distribution results in significant cogging torque reduction, which improves the machine's low-speed performance.

Stator windings can be either single-or double-layer and this selection is thoroughly dependent upon the desired machine performance characteristics. A single-layer CW is a selection with better fault-tolerance capability due to its high self-inductance and low mutual inductance [20-22]. On the other hand, a double-layer CW has lower air-gap MMF harmonic components, thereby smaller torque ripple and lower magnet eddy current losses [20-22].

Moreover, a double-layer CW has the best potential in terms of winding length reduction. Each slot contains coils from two different phases as shown in Figure 1.3(b), accordingly a single slot is only required to contain half of the number of conductors compared to single-layered windings, thus leading to a two-fold reduction, in the end winding length [19]. It is estimated that double-layer concentrated windings result in a three-fold reduction of winding length compared to a DW based upon the conductor slot area and elimination of phase-to-phase insulation for end windings [23]. The winding layouts for the single- and double-layer CWs are shown in Figure 1.3(a) and (b), respectively.

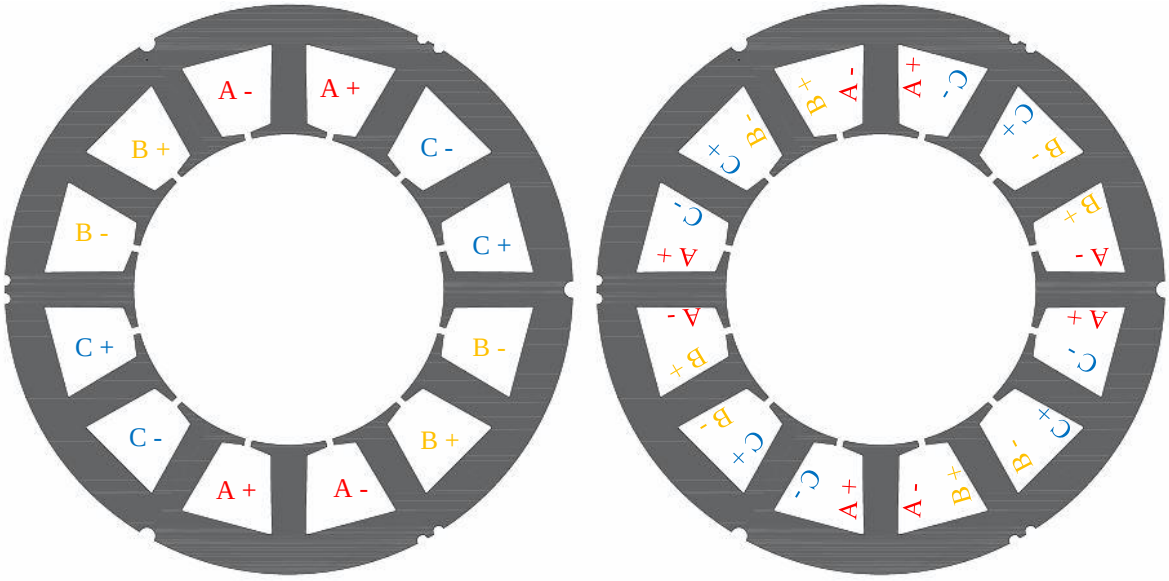

Figure 1.4 Concentrated windings (a) single-layer, (b) double-layer.

Slot-pole combination of the machine has a significant effect on its performance by directly determining its electrodynamic torque [24]. According to the mathematical investigation conducted in [24], which includes analysis on the winding factor, MMF assessment, and its harmonic analysis, it is suggested that a 12-slot/8-pole combination is preferred over other slot-pole combinations for higher torque density by its higher product of MMF to winding factor. Therefore a 12 slot/8 pole arrangement was selected for this thesis along with a double-layer, CW stator winding configuration based on the work conducted by Toulabi et al. [24, 25].

1.2 Performance Prediction and Analysis of PMSMs using Numerical Techniques

Accurate prediction and detailed electromagnetic analysis are important to ensure that a fabricated design will perform as expected. Since the electromagnetic phenomena of an electric machine can be expressed in mathematical form by Maxwell's electromagnetic equations, the analysis of such machines includes solving these equations either analytically or numerically. In

the analytical method, lumped electromagnetic models [26] or equivalent-circuit models [27] are used. On the other hand, finite differential and finite element methods (FEMs) are alternatives for numerical analysis of electric machines. [10].

The nonlinear characteristics of magnetic materials, saturation effects, and design complexities render analytical methods less applicable than numerical analysis methods. Among such numerical methods, the FEM is widely used because of its flexibility and accuracy. FEM can estimate the effect of armature reaction, winding inductances, core losses, and cogging torque of the permanent magnet (PM) machines accurately [28].

When utilizing FEM, the study domain is divided into finite elements of simple geometric shapes to minimize the complexity of a problem. Maxwell's equations, electrical coupling equations (external voltages) and mechanical coupling equations (mechanical movement) are then considered for each finite element. The time domain variables of these equations are handled by backward Euler method and form a large global matrix by assembling the element matrices. The nonlinear equations in the global matrix are solved by iterative methods such as Newton-Raphson to find their unknown independent variables. The general steps of finite element method (FEM) are as follows [28-34]:

a) Mathematical representation of the system
b) Mesh formation
c) Assignment of material properties to the various regions
d) Assignment of source of excitation and boundary conditions
e) Derivation and assembly of element matrix equations and global matrix
f) Solution of the equations for unknown variables
g) Post-processing or analysis of results obtained

FEM is either two-dimensional (2D-FEM) or three-dimensional (3D-FEM). The latter has higher computational complexity and requires a great deal of computations. The magnetic field in the air-gap of the radial-flux electric machine is virtually two-dimensional as it is radially distributed along the axial length and there is negligible fringing flux at the end of the axis. Therefore, use of 2D-FEM for most radial-flux rotating electric machines is justifiable [28]. Electromagnetic phenomena of an electric machine can be expressed mathematically by well-known Maxwell's electromagnetic equations in differential form.

Creating a proper mesh for the study domain in an optimal manner (for example to have high mesh density around highly saturated areas) is a vital factor in determining the accuracy of a FEM solution. A triangular element in 2D-FEM and a tetrahedron in 3D-FEM are widely used since any polygon in the 2D plane can be represented by combinations of triangles and any polyhedron in 3D as a combination of tetrahedrons [10]. The mesh shown in Figure 1.4 is constructed using a high density of triangular elements in the highlighted highly saturated areas around the permanent magnets.

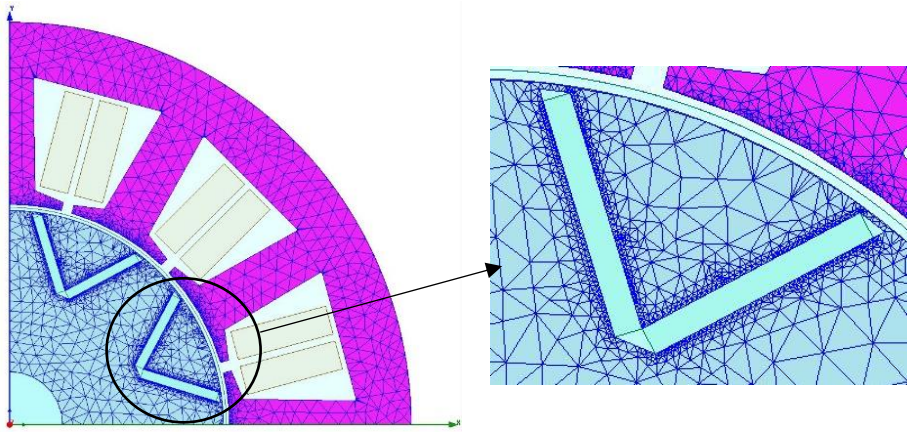

Figure 1.5 The FEM mesh of the rotor and stator.

In each finite element, corner points are called grid points or nodes and the main aim of the FEM is to solve for these unknown node potentials. Here each element has its own material properties and excitation may be present within the element or at the nodes.

Boundary conditions are imposed on the study domains of the electromagnetic field problems. They restrict the study domain to a certain extent, which in turn reduces the computational burden. Hence, the accuracy and efficiency of a FEM solution greatly depends upon appropriate boundary conditions. For example, most rotating electric machines have identical full or half pole pitches. In such cases, the modeling of one or a half pole pitch is sufficient to represent the field problem adequately. Thus, the size of the element matrix for an electric machine can be reduced significantly [31]. Generally, boundary conditions can be divided into the three main groups as Dirichlet boundary conditions, Neumann boundary conditions, and periodic boundary conditions. For a Dirichlet boundary condition, a specified value is assigned to the magnetic vector potential of a particular point, such that in a rotating machine; the outer stator yoke may have Dirichlet boundary condition of zero magnetic vector potential. The requirement in a Neumann boundary condition is that normal derivative of magnetic vector potential in the boundary must be zero. Hence the flux lines cross the Neumann boundary orthogonally. In a rotating electric machine, a periodic boundary condition relates two nodes that are one or multiple pole pitches apart [31].

The element matrices are formed by applying Maxwell's equations coupled with stator electrical circuit and rotor motion equations to the finite elements in the study domain. The large matrix of global system of nonlinear equations containing magnetic field equations, electrical, and mechanical coupling equations is resulted when all element matrices are combined. The size of the resulting matrix is determined by the total number of finite elements present in the study domain.

This matrix equations are solved simultaneously at each time-step using previous time-step results by using iterative methods such as Newton-Raphson. The inputs to the system are stator phase voltage (or current), rotor position, the geometry of the machine, and characteristics of materials. The stator current (or voltage), back-EMF, developed torque and speed, etc., are typical unknown quantities, which can be computed [10, 34].

1.3 Optimization-based Design

Static and dynamic performance characteristics of a machine can be further enhanced if design optimization algorithms are applied to help determine key parameters and dimensions. Design optimization requires a mathematical function (often referred to as an objective function), which can be a single-objective or multi-objective function. A nonlinear optimization algorithm then needs to be employed in order to minimize/maximize the stated objective function while satisfying thermal, mechanical, and material constraints [33].

The degree of conformity of an optimized IPMSM to the stated objectives largely depends on the properties of the nonlinear optimization algorithm used and the chosen design variables. Global optimization algorithms provide solutions with the highest conformity to defined OFs, while local optimizers find locally optimal solutions with a lower degree of conformity. Often the search area of a global optimizer is wider than that of a local optimizer. This leads to global optimizers being more computationally demanding than local optimizers [36]. The local techniques need an initial approximation, from which the algorithm, through an iterative procedure, finds the optimal solution evaluating the objective function a certain number of times. Global techniques do not require initial approximations since they explore all the space of variables seeking the minimum/maximum of the OF [35].

Optimal design modeling of PMSMs by adopting surrogate modeling techniques has been documented for both single-and multi-objective design optimization problems [33]. The surrogate models adequately capture the relationship between the design objectives and their inputs. Methods such as design space reduction and polynomial Response Surface Method (RSM) have been used to the design PMSMs [33].

The work presented in [36] simplified the shape of the slots in a surface mounted PM using design space reduction methods with the help of 17 design inputs, which included the material data, stator and rotor geometry, winding patterns, etc. Moreover, this method requires the selection of most suitable design variables and is usually completed with the help of statistical methods such as multi-regression screening methods [37].

The RSM model-based optimization utilized in in [38] optimized the constant power range by using three geometrical parameters of the permanent magnets. The main objective of this method was to find the functional relationship between the desired objective function and a set of input variables.

An optimal search algorithm can be divided into two categories: deterministic methods that find the optima algorithmically, and stochastic methods, which explore the solution space randomly. Among deterministic methods practiced in the area of machine design, Simplex Algorithm and sequential unconstrained minimization technique (SUMT) are the most popular ones [39]. SUMT first converts a constrained optimization problem into an unconstrained one by use of a penalty function and then applies sequential nonlinear programming for optimization. However, SUMT requires gradient calculations and is able to find the optimum results within a small number of iterations [40-45].

Simplex Algorithm is used as a local optimizing algorithm to optimally design IPM machines. Nonlinear Simplex Algorithm has been linked with Kriging interpolation method to minimize the cogging torque of an IPMSM in [46]. Moreover, a Simplex-based hybrid optimization algorithm is presented in [47] for notch-based optimization to reduce the machine's cogging torque, which may result in a reduced-vibration performance.

Stochastic methods are gradient-free and require more evaluations than deterministic methods. The stochastic nature of designing of an electric machine is capitalized by stochastic methods to design optimization using algorithms such as Genetic Algorithms and Particle Swarm Optimization (PSO).

GA is a widely used global optimizer for PMSM design optimization [48] and is developed based upon natural evolution. The work presented in [48] recruits the Kriging optimization algorithm using Latin Hypercube Sampling combined with GA to optimize a two-phase, in-wheel IPMSM to widen the machine's speed range. Three optimization algorithms using GA and three-weighted OFs are employed to design a 5-kW, 50-rpm radial flux SPMSM in [49] to minimize the weight of the machine. A GA-based multi-objective design optimization is presented in [50] to minimize the weight and maximize the efficiency of a 30-kW IPMSM for a compressor and weight minimization of an SPMSM alongside its housing combined with electromagnetic and thermal calculations is shown in [51].

The PSO algorithm is developed by simulating animals' social activities. It attempts to mimic the natural process of group communication to share an individual's knowledge when flocking, migrating, or hunting. If one member sees a desirable path to go, the rest of the swarm will follow it quickly. In PSO, this animal's behavior is replicated by particles with certain positions and velocities in the search space, wherein the population is called a swarm, and each

member of the swarm is called a particle. Starting from a randomly initialized population, each particle in PSO flies through the search space and remembers the best position it has seen. Members of a swarm communicate best-known positions to each other and dynamically adjust their own position and velocity based on these best-known positions. The velocity adjustment is based upon the historical behaviors of the particles themselves as well as their companions'. In this way, the particles tend to fly towards better and better-searching areas over the searching process [52].

Based on the work presented in [52], an intelligent model parameter identification method has used PSO for the PMSM parameter optimization using the traditional dq-model of PMSMs. PSO is used for automatic diagnosis of turn-to-turn short circuit faults in PMSM stator windings presented in [53], and in [33] it has been employed to optimize an SPMSM with five OFs including the weight and efficiency and compares the results with the GA outputs.

1.4 Scope of the Thesis

The motivation of this thesis is to conduct a comparative study on the predicted operating characteristics of a series of optimally designed concentrated-winding, 12 slot, 8 pole, V-shaped magnet IPMSMs. A local optimizer (nonlinear Simplex Algorithm) and a global optimizer (Genetic Algorithm) are used separately to determine the dimensions of each optimized machine based upon three distinctive objective functions. This makes the optimized machines suitable candidates for applications such as aerospace, electric vehicles and renewable energy that require minimized weights, high efficiency, or both. Besides using a local and a global optimizer, a multimodal optimization algorithm that can find all local and the global minima of a given, single- or multi-objective function is introduced. The main purpose of using different optimization algorithms and performing a comparative study is to have access to all or as many local optima as

possible, so the designer may select a suitable parameter with best fitting to his/her requirements in terms of conformity to objectives, lowest sensitivity, and lowest fabrication cost.

1.5 Thesis Organization

The thesis is divided into six chapters as described below:

- Chapter 2

  The analytical design procedure of a non-optimized machine, called “preliminary machine” is described solely based on conventional electrical and magnetic loading principles in full detail. Furthermore, the selection of suitable materials and derivation of the underlying equations for the machine’s dimensions are presented in order to determine the flux distribution inside the machine, and the desired developed torque and power.

- Chapter 3

  In this chapter, three optimization algorithms used to optimally design the V-shaped magnet IPMSM are introduced. GA and nonlinear Simplex Algorithms, as two widely-used global and local optimizers, are introduced and then a multimodal optimization algorithm is introduced to address multimodality of design objective functions. It is shown how these algorithms are used to obtain the optimal solutions fulfilling defined (OFs).

- Chapter 4

  In this chapter, GA and nonlinear Simplex Algorithm are used for design optimization of IPMSMs based on three distinctive OFs. Then, a comparative study is conducted using FEM to investigate the expected performance of the designed machines. The effect of tolerances applied to the design variables are investigated using sensitivity analysis.

- Chapter 5

  In this chapter, introduced multimodal optimization algorithm will be applied for the optimization of the IPMSMs. In addition, a comparative study is conducted, and chapter is concluded with the sensitivity analysis of the selected three designed machines, the introduction of the constructed machine, and the experimental performance validation for the fabricated machine.

- Chapter 6

  This chapter summarizes the contributions of the thesis as well as the key conclusions that are drawn from the studies conducted. In addition, Chapter 6 provides directions for future work on this topic to further extend the developed algorithms.

Chapter 2

Preliminary Design

Contents

2.1 Introduction

Designing an electrical machine is a complicated process performed using analytical equations considering its electromagnetic, mechanical, and thermal requirements. In this thesis, a non-optimized preliminary machine is designed based solely upon conventional electrical and magnetic loading principles [54]. This is important to (i) serve as a baseline for comparison with optimized machines, (ii) gain a general understanding about the ranges of the machine's dimensions, and (iii) use as a starting point for optimization algorithms that need an initial design known colloquially as a *seed*. In this regard, the machine's independent variables are arbitrarily selected within the desired/reasonable regions to find out their dependent variables. Selection of suitable materials and derivation of the underlying equations for the machine's dimensions are presented. However, it is necessary to use detailed numerical analysis, e.g., FEM, to verify the

quality of a design that is based upon electromagnetic analysis. The chapter concludes with a complete list of the specifications for the preliminary machine design.

2.2 Machine Specifications

IPMSMs are categorized according to the shape of the buried magnets. The analysis in [16,52] illustrates that among these categories, V-shaped IPMSMs have better overall performance in terms of average torque, reluctance torque, power/volume ratio, and power factor. By taking advantage of the reluctance torque contribution to the total developed torque, IPMSMs are commonly employed for applications that require a wide speed-range and high efficiency [56, 57]. Hence by taking the aforementioned advantages, this thesis investigates the design of V-shaped magnet IPMSMs. A 12 slot/8 pole arrangement is selected for this thesis along with a double-layer, CW stator winding configuration based on the advantages it offers. A schematic view of the rotor and stator structures of a double-layer CW, V-shaped magnet IPMSM are shown in Figure 2.1. The desired motor specifications are presented in Table 2.1. All the machine designs contained within this thesis have a rated power of 1 kW at 60 Hz.

TABLE 2.1
MACHINES COMMON SPECIFICATIONS

Parameter	**Value**	**Parameter**	**Value**
Output power	1 kW	Power factor	0.9
Synchronous speed	900 rpm	Conductor	AWG18
Rated voltage	225 V (rms)	Lamination	M19-29G
Rated current	3.5 A (rms)	Magnet	NdFeB35

2.3 Material Selection

The basic components of an IPMSM are its magnets, laminations, winding, and mechanical parts including ball bearings and shaft. The selection of these components must comply with certain requirements that are summarized in the following subsections:

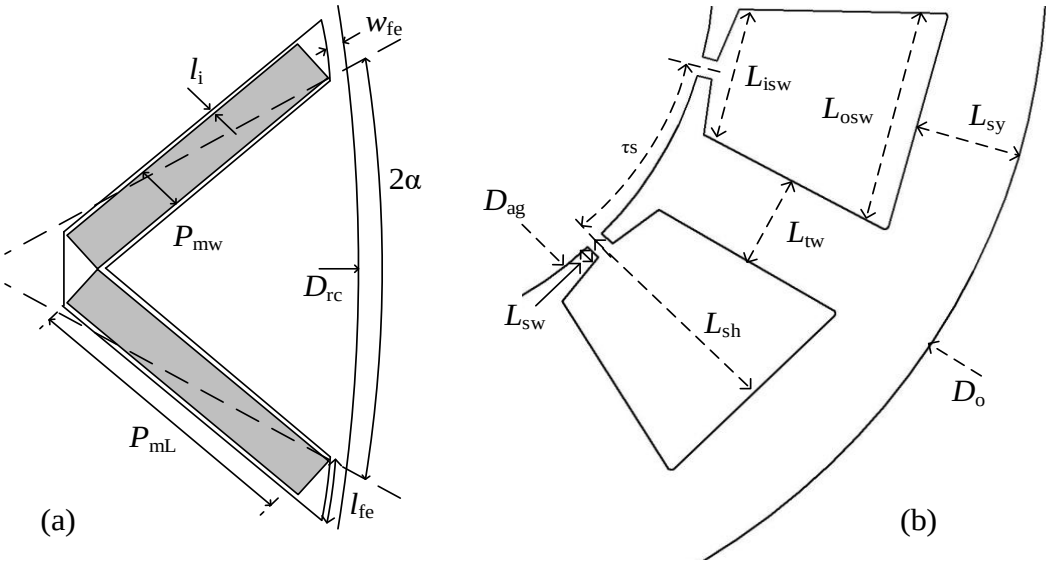

Figure 2.1 Schematic view of a V-shaped magnet IPMSM: (a) a sector of stator, (b) one pole of the rotor [58].

2.3.1 Magnet Selection

Permanent magnets in an IPMSM determine the overall performance of the machine. Based upon material composition, there are four types of commonly used and commercially available magnetic materials for IPMSMs [59]: Neodymium iron boron (NdFeB), Samarium Cobalt (SmCo), Ceramic (Ferrite: $BaFe_2O_3$ or $SrFe_2O_3$) and Alnico (AlNiCo).

In this thesis, NdFeB is selected as the magnet due to its high energy density, desirable coercivity, and high remnant flux density. These characteristics make the NdFeB a suitable candidate for wide speed-range and high-efficiency applications [60, 61].

The second quadrant of a magnetic material's *B-H* curve describes the conditions under which permanent magnets are used, and must be evaluated for the magnetic field strength and its ability to withstand demagnetization [59, 60]. The most important parameters on this curve are described and the values are selected based on the commercially available typical sintered (NdFeB35) magnets [61] as follows:

- Remnant flux density – (B_r)

  Remanence is the stabilized residual flux density remaining after reducing the external field from saturation to zero. This measures the strength of the magnetic field, and in this thesis, it is approximately 1.2 T for the selected magnet (NdFeB35).

- Coercive force – (H_c)

  Coercive force is the magnetic field intensity that must be applied to a magnetized material to remove its residual magnetism and is a measure of its resistance against demagnetization. For the selected NdFeB35 magnet, this value is equal to 899 kA/m.

- Energy density ($(B.H)_{max}$)

  The maximum energy product or $(B.H)_{max}$ of a magnet is equivalent to the area of the largest rectangle that can be inscribed under the normal *B*-*H* demagnetization curve as shown in Figure 2.2. This value is equal to 33 MGOe (or 263 kJ/m^3) for NdFeB35.

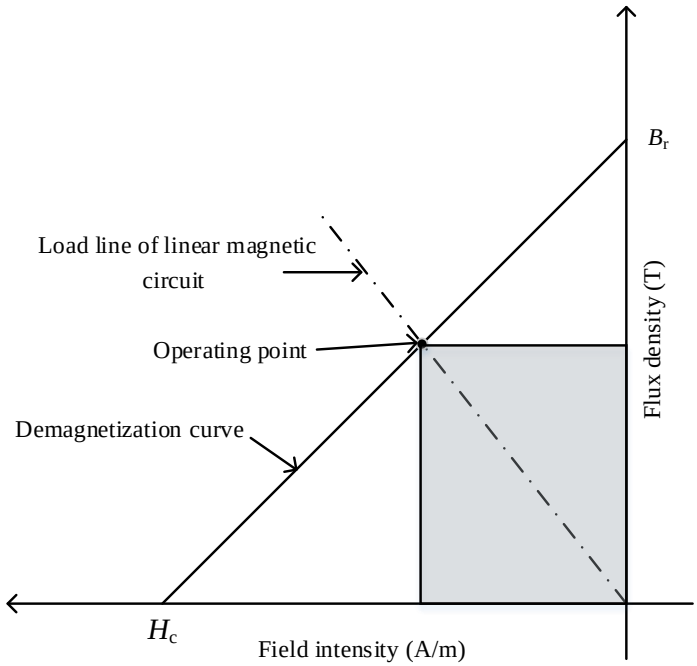

Figure 2.2 $(B.H)_{max}$ demonstration [62].

2.3.2 Laminations

Core (iron) losses of an electrical machine consist of eddy current and hysteresis losses. They directly affect the machine's efficiency and are a main source of heat generation within the machine [60]. In order to minimize hysteresis losses, both stator and rotor material must be selected to have narrow hysteresis loops. This implies that the stator and rotor material must have low coercivity, high permeability, and high saturation magnetization capability. Soft magnetic materials such as nickel-iron alloys satisfy these conditions and exhibit low hysteresis losses [64]. Silicon steel is one of the most important soft magnetic materials and has been selected as the lamination material since its electrical and magnetic properties make it well-suited for laminated cores where the flux direction is reversed or pulsates at high frequencies [65].

Eddy current losses occur in the core of a machine due to the induced non-uniform currents in the cross-section of the core by the alternating air-gap magnetic flux, tending to be the largest at the surface of the laminations. Resistivity of the laminations, which is mainly determined by the thickness of the material, greatly affects the magnitude of eddy current losses. Therefore, thinner laminations result in lower eddy current losses. The lamination thickness is normally selected to be larger than 0.014 inches (0.35 mm) for manufacturing simplicity unless the laminations are specifically used for high-frequency applications [66].

To achieve low core-losses, stator and rotor cores are made using laminated silicon steel (carbon steel alloyed with small quantities of silicon). This material is graded according to its losses denoted by an "M" number such as M19 or M27; material with a larger M number has higher iron losses but are lower in price. In this thesis, M19 is used for the lamination as it is one of the most cost-effective grades of silicon steels, and also can support low magnetic losses [67].

2.3.3 Stator Winding Material

Copper and Aluminium are commonly used as conductors by machine manufactures and have certain advantages and disadvantages compared with each other. The current density of copper is 30% higher than aluminium, while aluminium is markedly less expensive than copper [20]. A number of specialists consider copper as a superior conductor because of its resistivity, which is 63% lower than that of aluminium [68]. Additionally, copper has high conductivity, good mechanical strength, and relatively low-temperature coefficient of resistance [59]. Table 2.2 represents a comparison between the properties of different metals used as conductors [69].

TABLE 2.2
COMPARISON OF CONDUCTIVE MATERIALS

Conductor	E_c **(10^6 Siemens/m)**	τ **(10^{-8} Ω.m)**	T_c **(W/m.K)**	ρ **(g/cm^3)**
Silver	62.1	1.6	420	10.5
Copper	58.5	1.7	401	8.9
Gold	44.2	2.3	317	19.4
Aluminum	36.9	2.7	237	2.7
Brass	15.9	6.3	150	8.5

2.3.4 Shaft

A shaft is used to convey the generated mechanical power to the connected external load. The obvious material selection for the shaft of the machine is a non-ferromagnetic material in order to prevent flux leakage generated by the permanent magnets at the shaft, and prevent extra power losses due to the leakage flux path created at housing of the machine through shaft [58]. A shaft made of carbon steel is usually selected in machine fabrication as this type of shaft is stronger than aluminium and stainless-steel shafts [70].

2.3.5 Ball-bearings

Pedestal support to the rotating shaft of the motor and reduction of friction between the moving parts are provided using ball bearings. A ball bearing contains a housing with rolling ball

elements mounted within and is normally selected based upon the operation speed, space availability, location, machine power rating, and other considerations [71].

2.3.6 Material-based Design Constants

Table 2.3 presents the design constants taken from the material properties specified in the previous sections. These design constants are used during the design process to analytically obtain the dimensions of a machine based on the defined voltage, current, and power ratings.

TABLE 2.3
MATERIAL-BASED DESIGN CONSTANTS

	Parameter	**Symbol**	**Unit**	**Value**
Magnet	Magnet density	ρ_{PM}	kg/m^3	7500
	Remnant flux density	B_r	T	1.2
	Relative permeability	μ_r	-	1.05
Iron	Steel density	ρ_{Fe}	kg/m^3	7750
	Eddy losses constant	k_{eddy}	-	1.1903×10^{-6}
	Hysteresis losses constant	k_{hyst}	-	0.0031
	Steinmetz constant	B	-	1.9
Windings	Copper resistivity	τ_{Cu}	Ω.m	1.68×10^{-6}
	Copper density	ρ_{cu}	kg/m^3	8920

2.4 Machine Dimensions

2.4.1 Geometric Assessment

In this section, analytical equations are derived for geometric parameters presented in Figure 2.1. The following equation is used for the inner stator diameter [54]:

$$D_{ag} = \sqrt{\frac{S}{11k_{w1}B_m E_l L n_{rs}}} \tag{2.1}$$

Where S represents the apparent power in VA, k_{w1} is the winding factor and is equal to 0.866 for a 12-slot/8-pole double layer winding machine [58], B_m is the average flux density in T, E_l is the electrical loading and is equal to 30000 A/m, L is the stack length in m, and n_{rs} is the synchronous

speed in revolutions per second [54]. The mathematical relationships to calculate the rest of the parameters are as follows [58].

$$L_{\mathrm{isw}} = \frac{\pi(D_{\mathrm{ag}} + 2L_{\mathrm{sw}})}{Q_{\mathrm{S}}} - L_{\mathrm{tw}} \tag{2.2}$$

$$L_{\mathrm{osw}} = \frac{2A_{\mathrm{sl}}}{L_{\mathrm{sh}} - L_{\mathrm{sw}}} - L_{\mathrm{isw}} \tag{2.3}$$

$$D_{\mathrm{rc}} = D_{\mathrm{ag}} - 2\delta \tag{2.4}$$

$$D_{\mathrm{o}} = D_{\mathrm{ag}} + 2L_{\mathrm{sh}} + 2L_{\mathrm{sy}} \tag{2.5}$$

$$L_{\mathrm{sy}} = \frac{L_{\mathrm{sh}}}{2} \tag{2.6}$$

$$L_{\mathrm{so}} = k_{\mathrm{open}} \times L_{\mathrm{isw}} \tag{2.7}$$

$$\tau_{\mathrm{s}} = \frac{\pi D_{\mathrm{ag}}}{Q_{\mathrm{s}}} \tag{2.8}$$

$$C_{\mathrm{ea}} = (\frac{L_{\mathrm{sh}}}{2} + \frac{D_{\mathrm{ag}}}{2}) \times \frac{2\pi}{Q_{\mathrm{s}}} \tag{2.9}$$

$$P_{\mathrm{tl}} = 2(C_{\mathrm{ea}} + (L + 0.02)) \tag{2.10}$$

$$T_{\mathrm{ph}} = \frac{E \times \frac{p}{2}}{\omega_{\mathrm{e}}\ K_{\mathrm{w1}} L\ D_{\mathrm{ag}} (\frac{4B_{\mathrm{m}}}{\sqrt{2}\pi})} \tag{2.11}$$

$$n_{\mathrm{s}} = \frac{2\ T_{\mathrm{ph}}\ P_{\mathrm{h}}}{w_{\mathrm{l}}\ Q_{\mathrm{s}}} \tag{2.12}$$

In this thesis, the ratio of stator slot opening to the inner stator tooth tip thickness (k_{open}) is assumed to be equal to 0.15 in order to avoid slot openings that would be impossible to manufacture [58]. E, p, and ω_{e} denote the back-EMF's rms value (V), number of poles, and

electrical frequency (rad/s), respectively. Furthermore, the number of phases, winding layers, and slots are represented by P_h, w_l, and Q_s; the number of poles is denoted by p. The current rating and current density are used to calculate the per-conductor area and are consequently employed to calculate the slot area (A_{sl}) subject to a slot fill-factor of 0.4. According to [72], a slot fill-factor of 0.45 can be achieved for a concentrated winding by ordinary hand-winding methods. The idea behind the selected value of 0.4 is for the case that the winding has not been ideally wound, and there may still be some unused space in the slots.

It should be noted that slot openings are considered as straight lines under the assumption that the slot pitch is small compared to the inner stator diameter when developing (2.2) and (2.3), and stator yoke height (L_{sy}) is assumed to be half of the stator slot height (L_{sh}). L_{sw}, W_{fe}, and l_i are all kept constant and equal to 2 mm, 0.5 mm, and 0.05 mm, respectively, for all designed machines, while L_{fe} may vary and is a function of magnet width (P_{mw}) and constant air-gap around PM (l_i).

Windings' conductor size is selected based upon a current density of 4 A/mm^2 with no air circulation to ensure proper thermal characteristics. In addition, the split ratio of the machine is adjusted between 0.4 and 0.7 [73-75], to avoid additional thermal issues.

The references [58, 76] indicate that a machine must have a stator yoke height set to at least half of the stator slot height and the tooth width is adjusted to be at least 30% of the slot pitch in order to ensure mechanical rigidity.

The concentrated winding structure adopted in this thesis reduces the end-winding length of the machine as well as the associated copper losses [58]. An appropriate approximation of the end-winding length (L_{ew}) is essential to obtain a reliable efficiency estimate. The following calculations provide this approximation for the proposed machine design.

The vertical coil span (H) is approximated as follows.

$$H = L_{sh} - L_{sw} \tag{2.13}$$

L_{ew} is approximated using the following equations:

a) The number of series conductors (n_1) in one row to cover length H:

$$n_1 \cong \text{round}\left(\frac{H}{D_c}\right) \tag{2.14}$$

b) The number of rows for the specific number of slot turns (n_2)

$$n_2 \cong \text{round}\ \left(\frac{n_s}{n_1}\right) \tag{2.15}$$

$$\therefore L_{ew} \cong n_2 \times D_c \tag{2.16}$$

According to the aforementioned consideration, an additional 0.02 m of length is added to the stack length assuming the winding tolerances to calculate the per-turn length (P_{tl}) of the windings including the end-winding. Hence, the machine's per-phase winding resistance is given by (2.17) [58].

$$R = \frac{\tau_{Cu} T_{ph} \times (P_{tl})}{C_s} \tag{2.17}$$

2.4.2 Electromagnetic Governing Equations

The reliability of the machine design process relies heavily on the accuracy of the air-gap flux density calculation. The equation used to calculate the average air-gap flux density (B_m) is presented in (2.19) considering the Carter factor in (2.18). The simplified air-gap flux density waveform and its fundamental component are shown in Figure 2.3 [62].

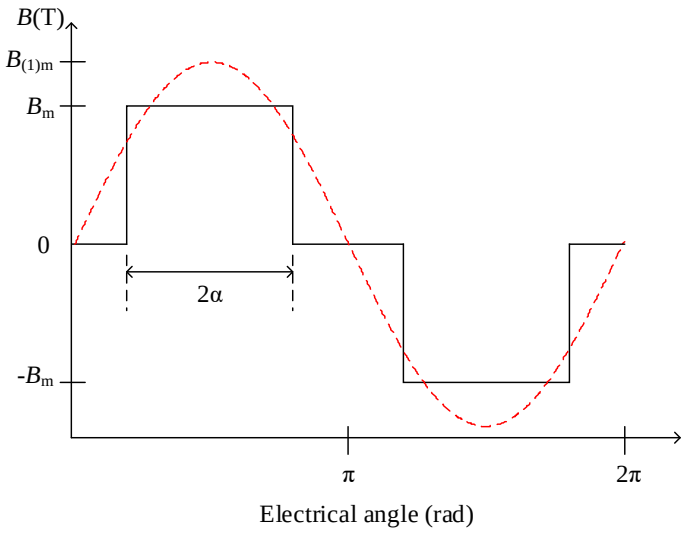

Figure 2.3 Air-gap flux density and its fundamental component.

$$k_c \approx \frac{\tau_s}{\tau_s - k\, L_{so}} \tag{2.18}$$

$$B_m = \frac{B_r - B_{sat} k_f \left(\frac{w_{fe}}{P_{mL}}\right) \times \left[1 + \mu_r \left(\frac{l_i}{P_{mw}}\right)\right]}{\left(\alpha_{mech} \frac{D_{rc}}{2P_{mL}} + 2\left(\frac{w_{fe}}{l_{fe}}\right) k_C \frac{\delta}{2P_{mL}}\right) \times \left[1 + \mu_r \left(\frac{l_i}{P_{mw}}\right)\right] + \mu_r k_c \frac{\delta}{P_{mw}}} \tag{2.19}$$

Where B_r is the remnant flux density of the magnet in T, α_{mech} (rad) represents half of the magnet pitch in mechanical degrees, μ_r is the relative permeability, and the stacking factor for the laminations is shown by k_f.

By applying Fourier analysis, the peak value of the fundamental air-gap flux density (Figure 2.4) can be calculated using (2.20). Equation (2.21) shows the air-gap flux density waveform as a function of the electrical magnet pitch (α), average air-gap flux density value (B_m), and electrical frequency (ω) in rad/s. Total harmonic distortion (THD) of the air-gap flux density waveform (B_{THD}) is calculated using (2.22), and the magnet pitch for which B_{THD} is minimized is calculated by setting the derivative of the B_{THD} with respect to α equal to zero. Accordingly, α is equal to 67.78 (elec. deg.) or (0.291 mech. rad).

$$B_{(1)\mathrm{m}} = \frac{4}{\pi} B_{\mathrm{m}} \sin(\alpha) \tag{2.20}$$

$$B(\alpha) = \frac{4B_{\mathrm{m}} \sin(n\alpha) \sin(n\omega t)}{n\pi} \qquad n = 1,3,5.... \text{odd} \tag{2.21}$$

$$B_{\mathrm{THD}} = \frac{\sqrt{\sum_{\mathrm{n}=3}^{\infty} \left(\frac{4B_{\mathrm{m}} \sin(n\alpha)}{\sqrt{2} \times n\pi}\right)^2}}{4B_{\mathrm{m}} \sin(\alpha) / \sqrt{2}\pi} \times 100\% \tag{2.22}$$

The developed steady state electromagnetic torque (T) in an IPMSM is shown by (2.23).

$$T = \frac{3p}{4} [\lambda_{\mathrm{pm}} i_{\mathrm{q}} + (L_{\mathrm{d}} - L_{\mathrm{q}}) i_{\mathrm{d}} i_{\mathrm{q}}] \tag{2.23}$$

Here the permanent magnet flux linkage is denoted by λ_{pm} (Wb), which is a function of the turn number and the air gap flux density waveform. The d-axis and q-axis inductances are denoted by L_{d} (H) and L_{q} (H) and are mainly a function of the rotor's pole structure [58]. The direct and quadrature current components are denoted by i_{d} and i_{q} (both in A) respectively. The steady state equations for d- and q-axis voltages for an IPMSM are given in (2.24) and (2.25).

$$v_{\mathrm{q}} = Ri_{\mathrm{q}} + \omega_{\mathrm{e}} \lambda_{\mathrm{pm}} + \omega_{\mathrm{e}} L_{\mathrm{d}} i_{\mathrm{d}} \tag{2.24}$$

$$v_{\mathrm{d}} = Ri_{\mathrm{d}} - \omega_{\mathrm{e}} L_{\mathrm{q}} i_{\mathrm{q}} \tag{2.25}$$

Here v_{q} and v_{d} represent the q- and d-axis voltages (V), respectively. From equations (2.22) to (2.25), it is shown that the developed torque and the required voltage for a specific operating point are mainly a function of the rotor's structure, the winding resistance, and the supplied frequency. The voltage phasor diagram of an IPMSM in d-q frame at steady state is shown in Figure 2.4, where the vector, $\boldsymbol{V}_{\mathrm{s}}$, is given by (2.26);

$$\boldsymbol{V}_{\mathrm{s}} = v_q + jv_d \tag{2.26}$$

In addition, Figure 2.5 shows the equivalent circuits in d-q reference frame in steady state. The maximum available line-to-line rms voltage on the designed machine's phases is 225 V.

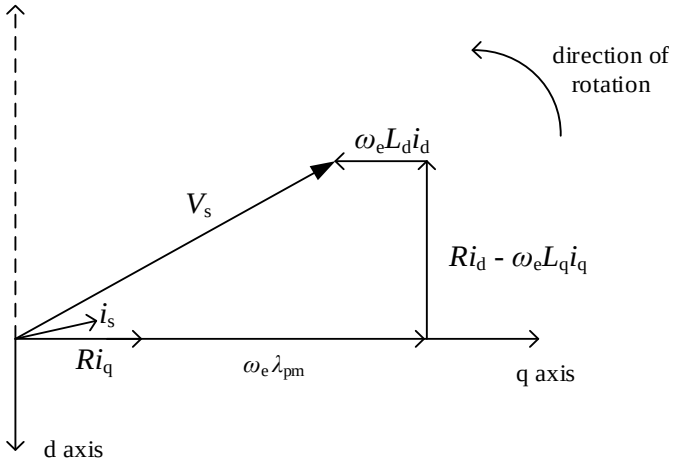

Figure 2.4 Voltage phasor diagram for an IPMSM.

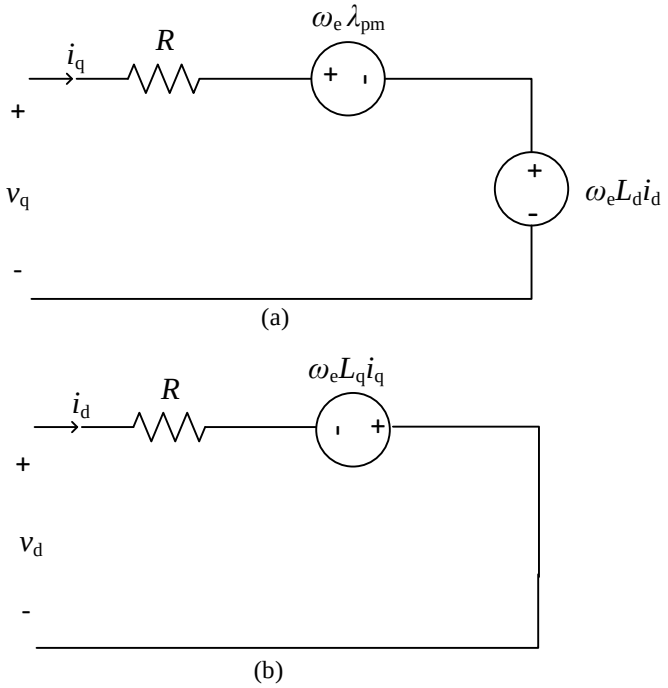

Figure 2.5 IPMSM equivalent circuits in steady state (a) q- axis (b) d- axis.

2.5 Analytical Weight, Loss, and Efficiency

The stator, rotor, magnets, and copper weights are given in (2.27) to (2.30), and the total active weight is calculated using (2.31). Hysteresis loss density in the stator and/or rotor is given by (2.32), where B_s is the peak flux density in the core. Similarly, the eddy current losses density in the stator and/or rotor is calculated in (2.33). Calculation of the total iron losses of stator/rotor

is then based on (2.34), where *m* is the weight of the analyzed portion (in kg) and is used to find the total iron losses of the machine based on (2.35) considering the iron losses components in the stator and rotor.

$$W_{\text{stator}} = (\frac{\pi L(D_{\text{o}}^2 - D_{\text{ag}}^2)}{4} - Q_{\text{s}} A_{\text{sl}} L)\rho_{\text{Fe}} \tag{2.27}$$

$$W_{\text{rotor}} = (\frac{\pi\, L(D_{\text{rc}}^2 - D_{\text{sh}}^2)}{4} - 2pP_{\text{mw}}\, P_{\text{mL}} L)\rho_{\text{Fe}} \tag{2.28}$$

$$W_{\text{magnet}} = (2pP_{\text{mw}}\, P_{\text{mL}}\, L)\rho_{\text{PM}} \tag{2.29}$$

$$W_{\text{Cu}} = \rho_{\text{Cu}}(Q_{\text{s}}\, n_{\text{s}} w_{\text{l}}(L + 0.02) + 6\,(C_{\text{ea}})\, T_{\text{ph}})C_{\text{s}} \tag{2.30}$$

$$F_{\text{weight}} = W_{\text{stator}} + W_{\text{rotor}} + W_{\text{magnet}} + W_{\text{Cu}} \tag{2.31}$$

$$P_{\text{hyst}} = k_{\text{hyst}} \omega B_S^{\beta} \tag{2.32}$$

$$P_{\text{eddy}} = k_{\text{eddy}} \omega^2 B_{\text{s}}^2 \tag{2.33}$$

$$P_{\text{iron}} = (P_{\text{hyst}} + P_{\text{eddy}})m \tag{2.34}$$

$$P_{\text{iron(total)}} = P_{\text{iron}\,\text{stator}} + P_{\text{iron}\,\text{rotor}} \tag{2.35}$$

$$P_{\text{Cu}} = 3I^2 R \tag{2.36}$$

$$P_{\text{loss}} = P_{\text{iron}} + P_{\text{Cu}} \tag{2.37}$$

$$\eta\ (\%) = \frac{P_{\text{out}}}{(\ P_{\text{out}} + P_{\text{loss}}\ )} \times 100 \tag{2.38}$$

2.6 Analytical Design Process

The conventional electrical and magnetic loading principles presented by equations (2.1) to (2.12) are used to analytically design a preliminary machine. Initially, a number of the machine's dimensions are selected arbitrarily within reasonable ranges. Additionally, the stack length (*L*) and

air gap length (δ) of the machine are selected as 0.05 m and 0.0015 m, respectively, and the tooth width (L_{tw}) is selected as 0.3 times the slot pitch (τ_s) of 0.0237 m. The magnet length (P_{mL}) and thickness (P_{mw}) of each pole are equal to 17 mm and 1.5 mm, respectively, to support the desired average air-gap flux density. Moreover, equating the expressions for L_{osw} in (2.3) and (2.39) is used to develop a second-order equation to solve the indicated variable, i.e., stator slot height (L_{sh}).

$$L_{osw} = \pi\left(\frac{D_{ag} + 2\,L_{sh}}{Q_s}\right) - L_{tw} \tag{2.39}$$

In addition, the magnetic flux density in the stator yoke (B_{sy}), and maximum flux density in the stator teeth (B_{ts}) are taken as 1.6 T. The specific magnetic loading, which is defined as the average total flux per unit area over the surface of the armature periphery of the machine, is selected as 0.7 T [58]. Specific electrical loading, which is the axial current per meter of circumference of the rotor, is selected as 30000 A/m for the design process.

The flowchart in Figure 2.6 shows the procedure to analytically design the machine using the describing equations in (2.1) to (2.39).

2.7 Preliminary Design Dimensions

The design process described in the previous sections is used to design a preliminary machine, and Table 2.4 demonstrates the dimensions of this non-optimized machine.

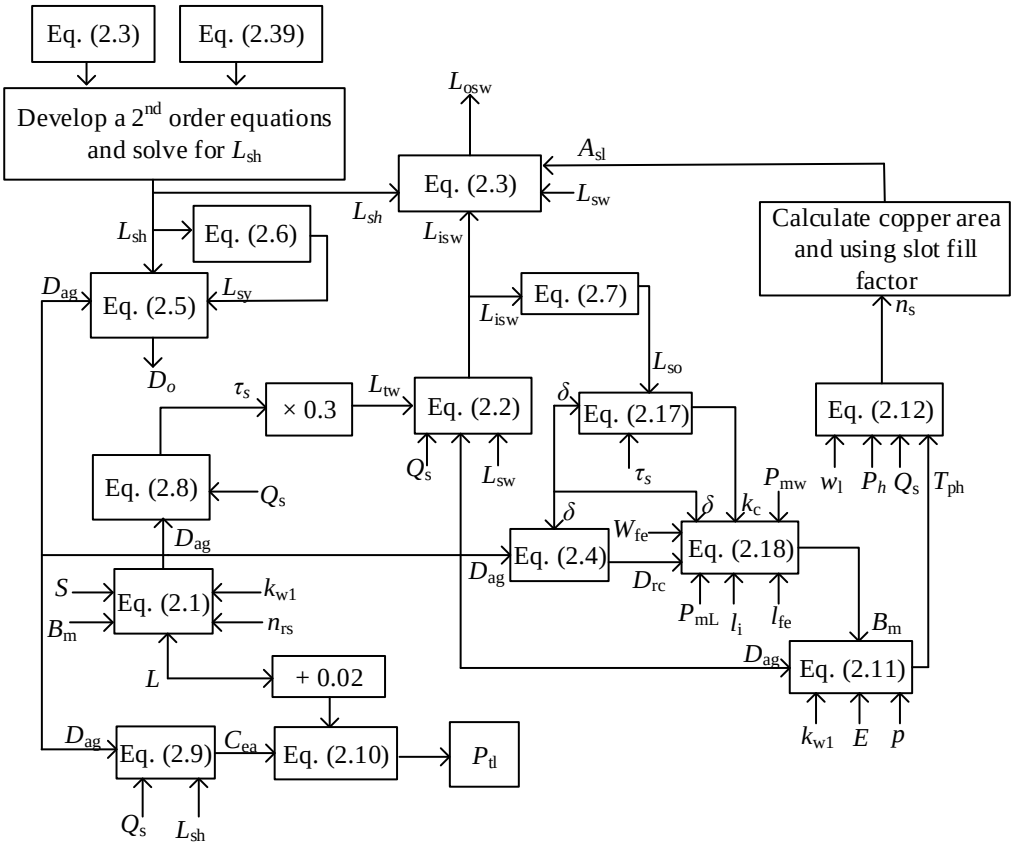

Figure 2.6 IPMSM's analytical design flowchart.

TABLE 2.4
MACHINE SPECIFICATIONS FOR A NON-OPTIMIZED PRELIMINARY DESIGN

Parameter	Unit	Value
Efficiency	%	92.88
Weight	kg	8.3238
L	m	0.0500
D_{rc}	m	0.0887
D_{ag}	m	0.0907
D_o	m	0.1780
δ	m	0.0015
L_{sh}	m	0.0291
L_{tw}	m	0.0071
L_{yh}	m	0.0146
L_{isw}	m	0.0177
L_{osw}	m	0.0246
L_{so}	m	0.0027
P_{mw}	m	0.0015
P_{mL}	m	0.0170
n_s	Turn	139

2.8 Closing Remarks

In this chapter, an initial IPMSM design was formulated, and it was shown how conventional electrical and magnetic loading principles are used to obtain the dimensions of a machine considering the voltage and current limitations for the desired output power. Different materials for laminations, magnets, and conductors were considered, so one can select suitable materials during the machine design procedure.

The design process began by developing the analytical equations based upon the desired power ratings, available voltage, and permitted dimensions for the machine. Additionally, the mechanical, thermal, and magnetic considerations were also taken into consideration during the design procedure, and finally, a non-optimized preliminary machine was designed and its dimensions along with its weight and efficiency at the rated conditions were introduced. It is worth noting that this preliminary machine is not optimized to fulfill any defined objectives, and its present dimensions only satisfy the basic conditions within the desired outputs and defined dimensions.

Chapter 3

Optimization Algorithms

Contents

3.1 Introduction

In this chapter, three optimization algorithms used to optimally design V-shaped magnet IPMSM are introduced. It is shown how these algorithms are used to obtain optimal solutions fulfilling defined Objective Functions (OFs). The main strategy of these optimization algorithms is primarily based on repeated evaluations of the OF and dynamical modifications of the trial points until the desired optimal objectives are achieved. The quality of the optimized results depends on the associated search region. The larger region is preferred over the narrower regions for the guaranteed best optimal results (maybe a global optimum). Local optimizers, such as the nonlinear Simplex Algorithm, are simple and efficient search methods that can find an optimal solution quickly. On the other hand, they are not necessarily capable of finding the global optimum, as the optimal result they find is directly a function of the initial search area [77]. Using a larger number of OF evaluations than local optimizers, global optimizers such as Genetic Algorithms are capable of finding global solutions [78]. As a disadvantage, global optimizers require more computational time than local optimizers [78, 79].

From a practical viewpoint, a machine designer may need access to as many optimized machine designs as possible to have more freedom in selecting the final model. Accordingly, the selection of the final design can be done taking into account performance indicators such as speed range, performance at the high speeds, sensitivity to parameter variations, relative cost of implementation, etc., which are not directly included in the defined OF. Accordingly, this leads to the need for a new optimization algorithm that is capable of providing the global as well as (all) the locally optimal results at the same time [80].

In this thesis, genetic and nonlinear Simplex Algorithms are introduced and used for optimizing a IPMSMs. Then, a multimodal optimization algorithm is used to address multimodality of design objective functions.

3.2 Genetic Algorithms

Genetic Algorithms are based on natural evolution. In this type of algorithms, the chance of survival is dependent on how well individuals fit the defined environment. Hence, the best-fitted individuals can generate a relatively large number of offspring (next generation of children) with better characteristics than their parents. Afterwards, new generations continuously improve their characteristics and evolve [77]. This adaptation to a given environment makes GAs a suitable candidate for a wide range of optimization problems including electric machine design [33].

The GA includes a series of steps to find the global optimum. Its main steps can be categorized as follows [81]:

- Initialization

  This involves generation of an initial population matrix, which contains randomly generated data points (N_i), usually referred to as “chromosomes”. The size of this matrix is normally large

enough to allow the algorithm to start with a wide search area. The evaluation of OF for each chromosome has to be completed before proceeding to the next stage of natural selection.

- Natural selection

  At this stage, N_p number of chromosomes ($N_i > N_p$) from the initial matrix is selected for generation of the next population. This initial selection of chromosomes can be done in two ways. One way is to select N_p chromosomes randomly from the initial matrix. Another way is to sort the initial matrix in an ascending order (in a minimization problem) according to their evaluated OF values and select the top N_p chromosomes, i.e., the ones with the lowest OF evaluations. Since the latter method guarantees the selection of best chromosomes, it is selected in this study. Usually, the number of chromosomes used to generate the new population is kept constant at N_p and modifications to the chromosomes are applied at the reproduction stage to filter the low-performing chromosomes and replace them with new chromosomes to breed the next generations.

- Reproduction

  In this step, two chromosomes are selected and used as parents to produce the offspring. This step can be conducted several times depending on the selected number of best-fit chromosomes among the N_p chromosomes by using the rank selection method, wherein the parents are selected by using the OF value rank assigned to each chromosome [81]. The breeding process of new children has two steps as, namely crossover and mutation.

The first step of the reproduction step is crossover and its role is to produce new children by combining selected parents from the mating pool. Each couple usually produces two offspring. The crossover process may be explained using parent A and parent B as shown in Table 3.1.

TABLE 3.1
TWO SELECTED PARENTS FROM THE MATING POOL

Bit point	1	2	3	4	5	6
Parent A	10	20	25	45	54	18
Parent B	7	8	9	10	11	12

According to a commonly used method of performing crossover, i.e., the single-point crossover method, the mating parents are cut at a randomly selected point and the resulting sections around the cut are swapped [81]. Accordingly, the parents will become offspring when the selection of the bit point is equal to 1 or *N*. Table 3.2 shows the results of a newly bred offspring A and offspring B. In this case, the respective values of parent A and parent B from the Table 1 are cut at bit point 3 and swapped.

TABLE 3.2
NEWLY BREADED OFFSPRING AFTER CROSSOVER STAGE

Bit point	1	2	3	4	5	6
Offspring A	10	20	**9**	**10**	**11**	**12**
Offspring B	7	8	**25**	**45**	**54**	**18**

A mutation step is used to recover the missing genetics or randomly disrupt them to preserve diversity among the genes and is conducted based on a mutation probability, which determines how often the changes to the parents or chromosomes should be performed. A user-specified mutation probability or rate determines the number of chromosomes taking part in mutation and should be a reasonable value to facilitate finding the global optimum. In this thesis, mutation is performed by replacing the existing values of two randomly selected bit points of each selected chromosome. This situation is demonstrated in Table 3.3 for the case that the selected values in columns 2 and 5 of the offspring B have been replaced by random values to perform mutation [81].

TABLE 3.3
OFFSPRING B AFTER MUTATION PHASE

Bit point	1	2	3	4	5	6
Offspring B	7	**8**	25	45	**54**	18
New offspring B	7	1	25	45	15	18

- Search Termination

The termination of any iterative method plays a vital role and has an impact on the quality of the final solution. The criteria below may be used for termination of a GA search.

a) Maximum number of iterations met

In this criterion, the GA process will be executed for a user-predetermined maximum number of generations.

b) No change in the fitness

In this termination criterion, the convergence is checked by comparing the most recent optimal OF values. The process terminates once this value lies within a pre-specified threshold, or at the maximum number of iterations if it is unable to satisfy the convergence criteria.

c) Elapsed time

To stop the GA process, the current execution time of the GA process is compared with a pre-specified maximum execution time. However, if the maximum number of iterations is reached or there is no change in fitness before the maximum adjusted elapsed time, the program is stopped [81].

The GA process discussed so far can be presented by the flowchart in Figure 3.1.

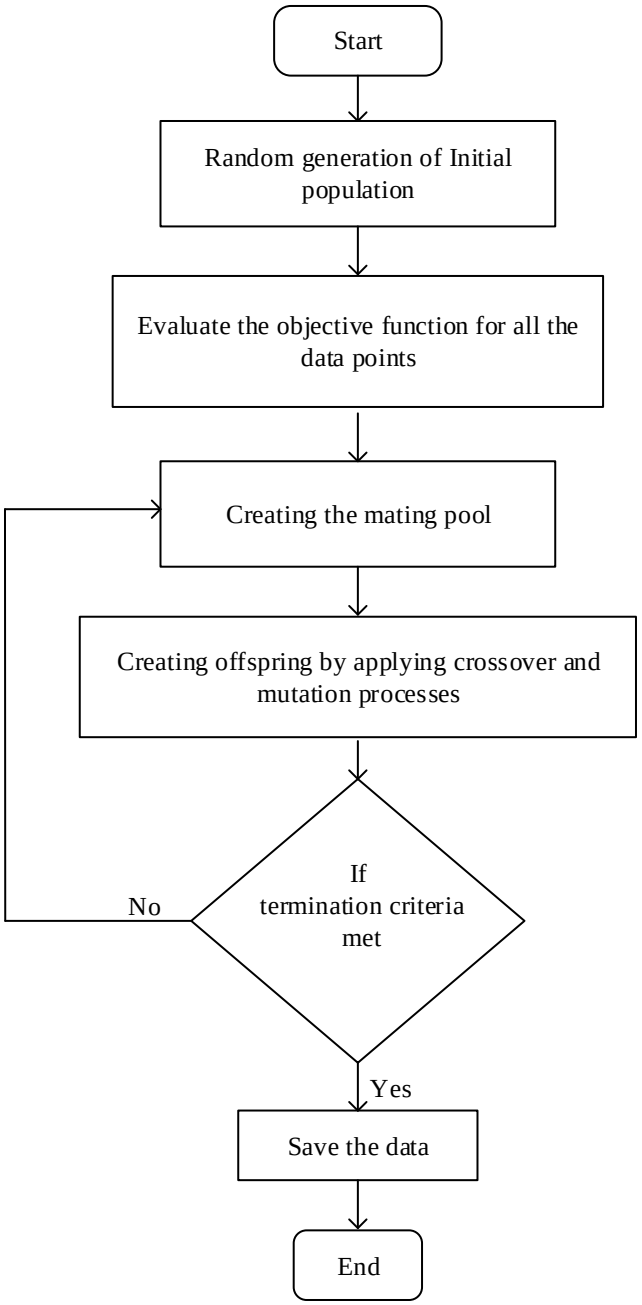

Figure 3.1 Flowchart of the GA process.

3.3 Nonlinear Simplex Algorithm

The nonlinear Simplex Algorithm by Nelder and Mead is a functional evaluation algorithm. From a geometric point of view, a simplex is a geometrical figure, in k dimensions, consisting of (k + 1) distinct points (or vertices) and all their interconnecting line segments, polygonal faces,

etc. In this regard, a two-dimensional simplex is a triangle and in three dimensions it is a tetrahedron. The fundamental principle of the Simplex algorithm uses the geometric concept of a simplex alongside with a series of operators called reflection, expansion, and contraction [82, 83].

The performance of the Simplex Algorithm is highly dependent on the local search area determined by the initial simplex [37]; therefore, this search area must be carefully specified. First, for multi-dimensional optimization, an initial simplex of (k+1) points in the k-dimensional space, where k represents the number of independent variables, is constructed. This creates an initial (k+1)×k matrix. The OFs are evaluated for each of the (k+1) vertices of the simplex. The point with the worst OF, X_W (maximum OF), and the point with the best OF, X_L (minimum OF), are then identified. Then, to find a better point that gives a better OF value, the algorithm iteratively updates the worst point (X_W) through four steps of (1) reflection, (2) expansion, (3) one-dimensional contraction, and (4) multiple contractions. These steps can be exemplified using the figure of a tetrahedron as shown in Figure 3.2.

1. Evaluate the OF values $f(X)$ of the vertices of the simplex and order them as:

   $f(X_L) < f(X_1) < \ldots < f(X_N) \ldots < f(X_s) < f(X_W)$

   Where X_s represent the second worst OF given point.

2. Reflection:

   Reflects the X_w through the centroid point (X_g) of the other k best points, to obtain a reflected point (X_r) and check for the condition of $f(X_L) < f(X_r) < f(X_s)$. Satisfaction of this condition allows the algorithm to obtain the new simplex by replacing the X_w by X_r and goes to step 1.

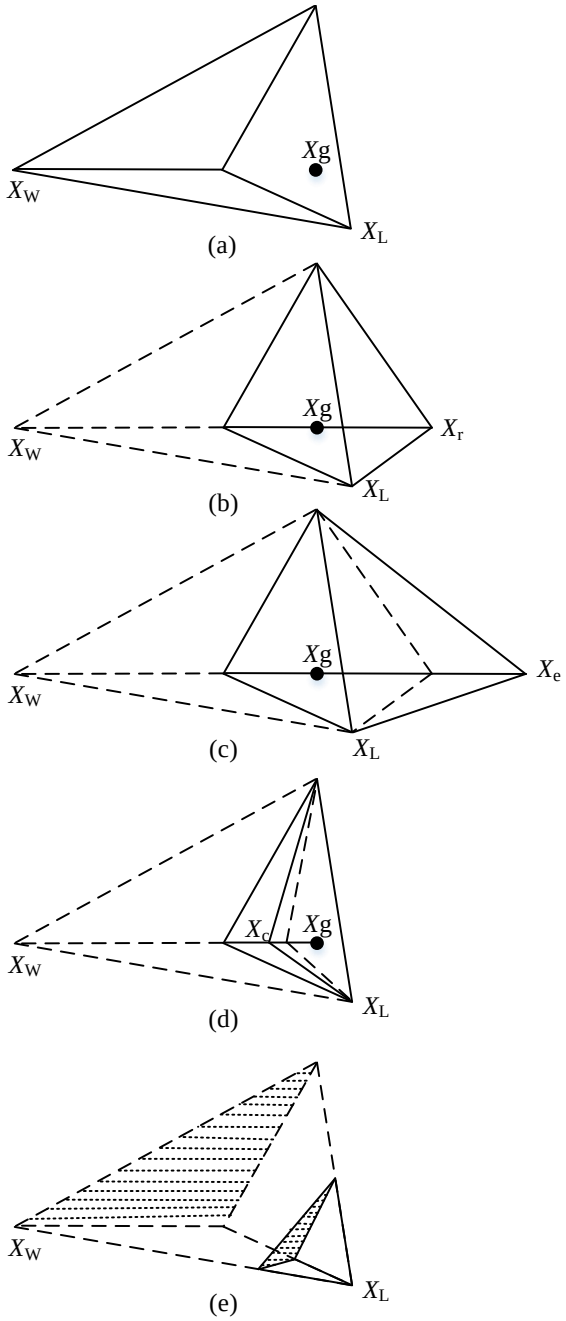

Figure 3.2 Steps for the downhill Simplex Algorithm. (a) initial simplex (here a tetrahedron), (b) reflection away from the high point, (c) expansion away from the reflected point to the new point X_e, (d) contraction along one dimension from highest point X_W to the new point X_C, (e) a contraction along all dimensions towards the low point [83].

3. Expansion:

   Expansion point (X_e) is calculated when the reflection point is the best point of the simplex, that is $f(X_r) < f(X_L)$. The OF value of point X_e is calculated and decisions are made as follows:

- if $f(X_e) < f(X_r)$, obtain the new simplex by replacing the X_w by X_e and go to step 1.
- if $f(X_e) > f(X_r)$, obtain the new simplex by replacing the X_w by X_r and go to step 1.

4. 1-Dimensional contraction

   When $f(X_r) > f(X_s)$, contraction point (X_c) is calculated through the direction of X_w and X_g. Then new simplex is constructed when the condition $f(X_W) > f(X_c)$ is satisfied by replacing X_w by X_c and goes to step 1.

5. Multiple contraction

   At the beginning of this stage, the reflected point is the worst point, that is $f(X_r) > f(X_W)$. In this case simplex contracts along with all dimensions toward the existing best point X_L to modify its shape and goes back to 1 [85].

In a multi-dimensional optimization algorithm, it is possible to check the convergence as soon as the decrement in the function value is fractionally smaller than some defined tolerance value. This tolerance value can be computed using the fractional value of the OF value from its highest to lowest values at each iteration and the algorithm iterates until convergence criterion is met or maximum iterations are reached [83].

3.4 Multimodal Optimization Algorithm

A multimodal optimization algorithm is introduced in this section, which is capable to find all the local optima of a multimodal, black-box, nonlinear OF. The developed multimodal optimization algorithm is based on an adaptive sampling of the OF to be optimized [84-86]. Since the algorithm only requires OF samples, which can be easily obtained using direct evaluation or computer simulations, it is also suitable for black-box optimization problems where an explicit, closed-form OF is unattainable [87].

The developed algorithm has three distinct stages of initialization, localization, and mesh refinement as shown in the following pseudo-code for an *N*-variable optimization problem.

- STEP 1: Initialization
  a) Generate a uniform set of n_i, sample points for variable x_i. This creates a mesh of points (i.e., different samples of the vector of variables to be optimized).
  b) Evaluate the OF for the generated points.
- STEP 2: Localization

  Determine the points in the mesh whose OF value evaluations are less than those of all the points immediately surrounding them. Localization identifies hyper-cubes (rectangles in 2D) surrounding middle points with lower OFs than the points on the boundaries of the hypercubes.
- STEP 3: Mesh refinement
  a) Increase the density of points in the localized area(s) by adding sample points to these areas only. New points will be added equidistantly for each variable.
  b) Evaluate the OF for the newly added points, and check the convergence.
  c) Terminate if convergence criteria are met.
  d) Proceed to STEP 2 otherwise.

The steps of the developed optimization algorithm are best exemplified visually using a two-variable problem. The algorithm is, however, fully capable of solving multi-variable optimization problems. The optimization procedure through this algorithm can be investigated using Himmelblau's two-variable optimization problem stated below [88]:

$$\begin{aligned} &\min f(x_1, x_2) = (x_1^2 + x_2 - 11)^2 + (x_1 + x_2^2 - 7)^2 \\ &-5 \le x_1 \le +5 \quad -5 \le x_2 \le +5 \end{aligned} \tag{3.1}$$

The defined OF in (3.1) has four locally optimal solutions in the given intervals that are located at (-3.78, -3.28), (+3.58, -1.85), (+3.0, +2.0), and (-2.8, +3.13) as denoted by red dots on the function's contour plots in Figure 3.4. Figure 3.4(a) shows the initial set of points uniformly placed in the search area. Eleven samples are chosen along each variable in this example. Figure 3.3(a) also shows four rectangular localized areas. Each of these areas contains a point in the middle with a lower OF value than those of the points on the sides of the rectangle surrounding it, thereby denoting a small valley within the localized area. Figure 3.3(b) shows the additional points that are inserted in each localized area to increase the estimation accuracy of the surrounded local minima. Figure 3.3(c) shows smaller localized areas that are determined upon evaluation of the newly added points. Figure 3.3(d) shows another iteration of mesh refinement resulting in smaller local areas closely surrounding each local minimum. Convergence may be determined after a given number of points are evaluated or when a local area becomes smaller than a certain threshold.

By focusing its search effort only in the localized areas where local minima exist, the developed algorithm avoids the unnecessary computational burden of brute force methods such as Monte-Carlo or sequential search algorithms. To ensure that a reliable estimation of the OF surface is achieved, a suitable number of initial points must be used. A larger number of initial samples results in a finer initial estimation of the OF surface at the expense of a larger number of OF evaluations.

For the multimodal optimization of expensive OFs, the developed algorithm may be executed on a parallel platform or interpolations may be used to relieve the computation of many intermediately inserted points during mesh refinement [86]. In machine design optimization, the practice of choice is to use the machine's governing equations for its optimization and to perform finite-element method (FEM) only on the finalized designs.

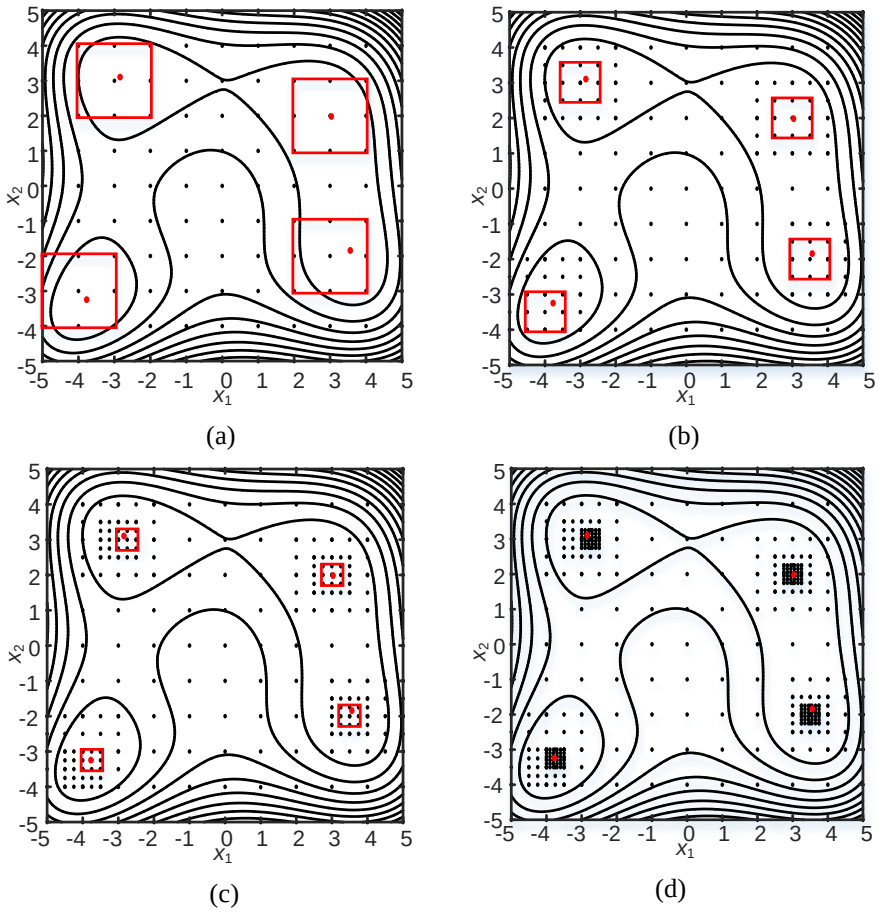

Figure 3.3 Multimodal optimization of Himmelblau's function (a) initial mesh, (b) second iteration (c) third iteration (d) fourth iteration.

3.5 Closing Remarks

In this chapter, three optimization algorithms suitable for machine design studies were introduced. Two of the introduced algorithms are well-known approaches and have been practiced for optimization problems for a long time, while the third one is a new optimization approach capable to simultaneously find all the local and global optima of a defined OF.

GA as a global optimizer tries to find the best conformity to the desired OF by searching through the wide search area with large trial points. Hence, it requires comparatively larger time than local optimization algorithms. On the other hand, the nonlinear Simplex Algorithm as a local

optimizer searches quickly within a small search area to find the local optimal solution and its output is greatly dependent on the initial searching area.

Although the global optimum result obtained by GA is normally preferred over the local optima obtained by the nonlinear Simplex Algorithm, the introduced multimodal optimization algorithm provides the designers with an opportunity to have access to all local and global optima at the same time. Accordingly, the designer may select an optimal solution that is not necessarily superior in terms of the OF value and is recommended due to other properties not directly included in the defined OF. However, depending on the area and density settings, the multimodal optimization approach requires a larger computational time than the other two algorithms (GA and Simplex).

Chapter 4

Design Optimization of IPMSMs using GA and Nonlinear Simplex Algorithms

Contents

4.1 Introduction

Design optimization of electric machines has been extensively practiced during recent decades. Electric machine design optimization starts with identifying the design variables and the design constraints. An objective function, which may comprise a single objective or weighted combination of objectives, has to be defined and used to obtain optimal results while keeping other technical indices and constraints within acceptable ranges [89].

In this chapter, two well-known optimization algorithms, namely GA and nonlinear Simplex Algorithm, are used for design optimization of IPMSMs based on three OFs. Then, a comparative study is conducted using the Finite Element Method (FEM) to investigate the expected performance of the designed machines. The effect of tolerances applied to the design variables are investigated using sensitivity analysis.

4.2 Optimization Setup

4.2.1 Independent Variables

Six independent variables along with their respective ranges are reported in Table 4.1. Furthermore, Table 4.2 shows the imposed constraints during the design optimization procedure considering thermal, mechanical, and magnetic limitations [60]. According to [90] and to prevent high temperatures and insulation problems, the maximum current density must be less than 7 A/mm^2. In this thesis, the current density is set to be 4 A/mm^2 to allow proper thermal behavior as well as to obtain an acceptable efficiency. The split ratio is an important factor to ensure acceptable thermal characteristics of the machine and is normally set between 0.4 to 0.7 [5]. The average air gap flux density (B_m) is set to 0.7 T to provide sufficient torque density for the machine without saturating the teeth and shoes of the stator.

TABLE 4.1
DESIGN VARIABLES

Variable	Minimum	Maximum
Stack length (L)	0.03 m	0.05 m
Air gap length (δ)	0.00085 m	0.0015 m
Stator slot height (L_{sh})	0.015 m	0.036 m
Stator tooth width (L_{tw})	0.0095 m	0.017 m
PM thickness (P_{mw})	0.002 m	0.004 m
PM length (P_{mL})	0.01 m	0.07 m

TABLE 4.2
IMPOSED CONSTRAINTS BASED ON MECHANICAL, THERMAL, AND MAGNETIC CONSIDERATIONS

D_0	$D_0 \leq 0.2$ m
L_{sy}	$L_{sy} \geq (L_{sh}/2)$
L_{tw}	$L_{tw} \geq 0.4\tau_s$
L_{isw}	$L_{isw} \geq (0.02/k_{open})$
L_{so}	2 mm $\leq L_{so} \leq$ 3 mm
J	4 A/mm^2
S_r	$0.4 < S_r < 0.7$
B_m	0.7 T

4.2.2 Objective Functions

In this section, three OFs are introduced to minimize (i) the total active weight of the machine (F_{weight}), and (ii) the electromagnetic losses (F_{loss}) both as single OFs, and (iii) a combination of total active weight of the machine and its electromagnetic losses simultaneously. Three OFs are shown in (4.1)-(4.3), respectively.

$$\min \text{OF}_1 = F_{\text{weight}}(L, \delta, L_{\text{sh}}, L_{\text{tw}}, P_{\text{mw}}, P_{\text{mL}}) \tag{4.1}$$

$$\min \text{OF}_2 = F_{\text{loss}}(L, \delta, L_{\text{sh}}, L_{\text{tw}}, P_{\text{mw}}, P_{\text{mL}}) \tag{4.2}$$

$$\min \text{OF}_3 = \lambda \cdot F_{\text{weight}}(L, \delta, L_{\text{sh}}, L_{\text{tw}}, P_{\text{mw}}, P_{\text{mL}}) + F_{\text{loss}}(L, \delta, L_{\text{sh}}, L_{\text{tw}}, P_{\text{mw}}, P_{\text{mL}}) \tag{4.3}$$

The F_{weight} and F_{loss} are functions of the machine's independent design variables. Mechanical losses are ignored in the analysis, while the DC copper losses, iron losses are taken in to account in F_{loss}. This F_{loss} is specifically defined to increase the efficiency of the machine and maintain it within the IE4-Super Premium efficiency standards. In order to fulfill the efficiency requirements, the phase current of the machine is specified in such a way to keep the analytical efficiency above 90% taking into account the driver's voltage ratings, output power of 1 kW AT 60 Hz electrical frequency, and power factor of 0.9 for all of the designed machines. Furthermore, the weighting factor λ is used in (4.3) to adjust the relative contribution of each sub-objective to the overall objective function OF_3. A larger λ gives a larger emphasis to the weight OF and vice versa. λ is set to 9.0 in order to nearly equalize the contributions of the weight (~8 kg) and losses (~72 W) to the overall OF.

4.2.3 Application of Optimization Algorithms

(a) Genetic Algorithms

In this algorithm, twenty different initial populations are generated with sizes varying from 100 to 2000 with increments of 100. Then the first 80% of the initial population members are selected after sorting them in ascending order by their OF values. At the reproduction step, (80%, 60%, and 40%) of chromosomes from the mating pool are selected by the rank selection method to perform single-point crossover and afterward mutation is performed for (1%, 5%, and 10%) of selected chromosomes in the mating pool. This selection of different proportions of chromosomes from the mating pool is to check the dependability of the optimal results on these algorithm parameters and to make sure that true globally optimal results are obtained. Finally, the process stops once the initially determined maximum number of iterations (100) is met. It was observed through the results that the dimensions of the machines are not significantly affected, and relatively similar designs are resulted even when the maximum number of iterations is above 100. Accordingly, and to save the computational time, the maximum number of iteration is set to 100.

In a minimization function, the OF values must decrease with the iterations as the solution moves towards the optimal solution. This condition is verified by the values obtained from the program as shown in Figures 4.1 to 4.3 for three different OFs.

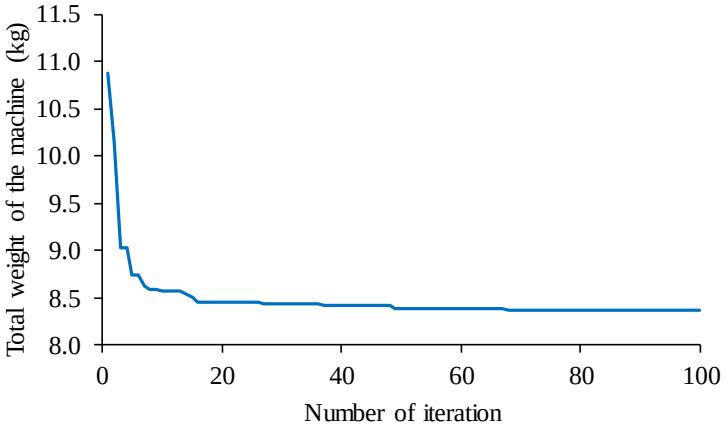

Figure 4.1 OF evaluation during the weight minimization using GA.

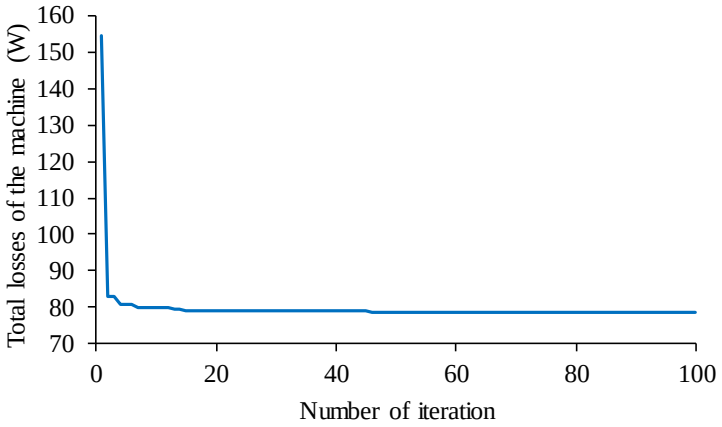

Figure 4.2 OF evaluation during the loss minimization using GA.

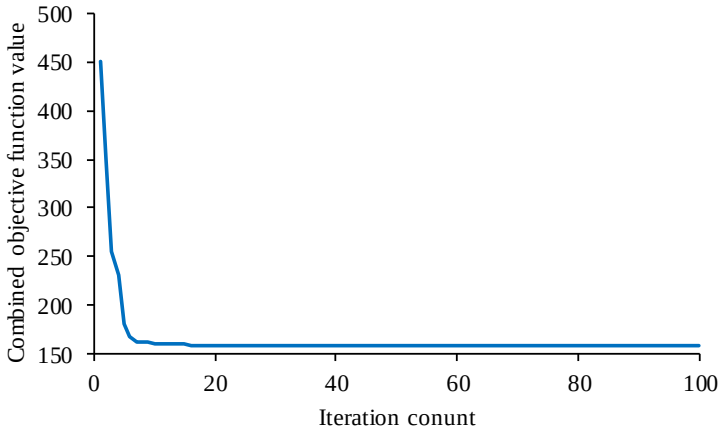

Figure 4.3 OF evaluation during the combined weight and loss minimization using GA.

(b) Nonlinear Simplex Algorithm

A similar optimization procedure is conducted using the nonlinear Simplex Algorithm; the local optimizing algorithm is initiated with a 7×6 matrix as there are six independent variables in the considered machine design problem. As the initial simplex significantly affects the performance of this algorithm, the dimensions of the preliminary design are used as the starting point to generate the initial matrix. However, the preliminary design has no unique dimensions as its independent variables are selected by designer arbitrarily within their respective ranges. Hence it has a direct influence on the final results of the Simplex algorithm.

In the Simplex Algorithm, variables are adjusted to obtain a design with best conformity to the assigned OF [83] in a local sense. The algorithm stops when 5000 iterations are reached or once to relative tolerance, r_{tol}, is lower than 1×10^{-10} indicating convergence. This fractional tolerance (r_{tol}) is calculated according to (4.4) [80].

$$r_{\text{tol}} = 2\times|f(\text{highest})-f(\text{lowest})|/|f(\text{highest})+f(\text{lowest})| \tag{4.4}$$

where *f*(highest) represents the highest OF value and *f*(lowest) shows the lowest OF value in each iteration.

Simplex is an unbounded optimization algorithm; i.e., the variables may take on any real value. In order to have design variables within the predetermined ranges, modifications have to be made to the initial and subsequent matrices using a limiter. For example, one may use (4.5) to convert an unbounded variable x' to a bounded variable $X \in [X_{\text{lower}}, X_{\text{upper}}]$.

$$X = (X_{\text{lower}}+X_{\text{upper}})/2+[(X_{\text{lower}}-X_{\text{upper}})/2]\times\sin(x') \tag{4.5}$$

In (4.5) X_{upper} and X_{lower} represent the upper and lower limits of the independent variable, respectively. After such Simplex and GA-based design exercises, the obtained dimensions of the

optimal designs alongside with their respective total active weights, losses, and efficiencies are presented in Table 4.3.

TABLE 4.3
SPECIFICATIONS AND DIMENSIONS FOR THE SEVEN DESIGNED MACHINES

Parameter	Unit	Preliminary	Genetic Algorithm			Simplex Algorithm		
			Min. weight	Min. loss	Combined objective	Min. weight	Min. loss	Combined objective
Weight	kg	8.3238	7.2773	7.7904	7.4287	7.4290	7.9082	7.6068
η_{Peak}	%	92.88	92.86	93.37	92.92	92.51	93.21	93.06
L	m	0.05	0.0331	0.0495	0.0369	0.0343	0.0499	0.0403
D_{rc}	m	0.0887	0.1086	0.0883	0.1027	0.1071	0.0878	0.0982
D_{ag}	m	0.0907	0.1115	0.0912	0.1056	0.1095	0.0908	0.1011
D_o	m	0.178	0.1996	0.1753	0.1930	0.1988	0.1761	0.1888
δ	m	0.0015	0.00145	0.0014	0.00145	0.00121	0.00150	0.00146
L_{sh}	m	0.0291	0.0294	0.0281	0.0292	0.0298	0.0284	0.0293
L_{tw}	m	0.0071	0.0117	0.0096	0.0114	0.0114	0.0095	0.0105
L_{yh}	m	0.0146	0.0147	0.0140	0.0146	0.0149	0.0142	0.0146
L_{isw}	m	0.0177	0.0185	0.0154	0.0173	0.0183	0.0153	0.0170
L_{osw}	m	0.0246	0.0329	0.0289	0.0318	0.0315	0.0280	0.0298
L_{so}	m	0.00265	0.0028	0.0023	0.0026	0.0027	0.0023	0.0025
P_{mw}	m	0.0015	0.0025	0.0025	0.0022	0.0020	0.0021	0.00225
P_{mL}	m	0.017	0.0180	0.0140	0.0190	0.0180	0.0170	0.0170
n_s	Turn	139	171	140	162	168	139	155
R	Ω	2.316	2.5175	2.3034	2.4433	2.4965	2.3051	2.3957
λ	-	-	-	-	9	-	-	9
P_{Cu}	W	77.65	81.18	77.05	79.14	80.56	77.51	78.94
P_{Iron}	W	4.93	4.81	4.99	5	5.05	4.79	4.81

With the knowledge of these optimal solutions, the designer can embark on a detailed electromagnetic assessment of the optimally designed machines to compare them not only from the OF viewpoint but also from other aspects not directly included in the OF. In the next section, such comparative assessment is carried out for the six optimally designed machines and the preliminary designed machine.

4.3 Comparative Study

4.3.1 Dimension, Efficiency, and Weight Comparison

According to Table 4.3, the preliminary design has the largest stack length of 5 cm and shortest stator outer diameter of 17.8 cm. The minimum-weight GA design has the shortest stack length of 3.31 cm, and the largest stator outer diameter of 19.96 cm. The efficiency of the minimum-loss GA design is 0.5% and 0.16% larger than the preliminary and minimum-loss Simplex designs, respectively. The iron losses are very close for all machines at around 4.8 W to 5 W, as they are recorded in low speeds. Copper losses vary between 77 W to 81 W resulting in different efficiencies. The minimum-weight GA design shows 1.0465 kg and 0.1517 kg less weight compared to the preliminary and the minimum-weight Simplex designs, respectively. The efficiencies and weights of the combined-objective designs for GA and Simplex Algorithms are within their minimum-weight and minimum-loss designs; the combined-objective GA design is 0.1781 kg lighter and 0.14% less efficient compared to its Simplex counterpart. As expected the (global) GA designs show the highest conformity to their respective objectives.

4.3.2 Analysis of other Performance Indicators using 2D Finite Element Method

For a more accurate electromagnetic analysis of the machines, precise magnetic properties of the utilized materials must be taken into account. In addition, the effect of harmonics in materials and air-gap should be considered as well. In order to fulfill these requirements, once the optimized machines are obtained detailed 2D-FEA simulations are necessary to be conducted to accurately compare and predict their performances at various operating points. FEA- based simulation is a highly accurate method to predict the performance of the machines prior to experimental studies as it considers slotting effects, inductance variations, high-frequency losses, and other non- linear properties over wide range of operating conditions. The geometries of the designed machines are

built in ANSYS-Maxwell and a series of finite-element method (FEM) are conducted. Figure 4.4 shows the structures and the flux density distributions at rated power and speed using ANSYS-Maxwell 2D analysis for the seven designed machines.

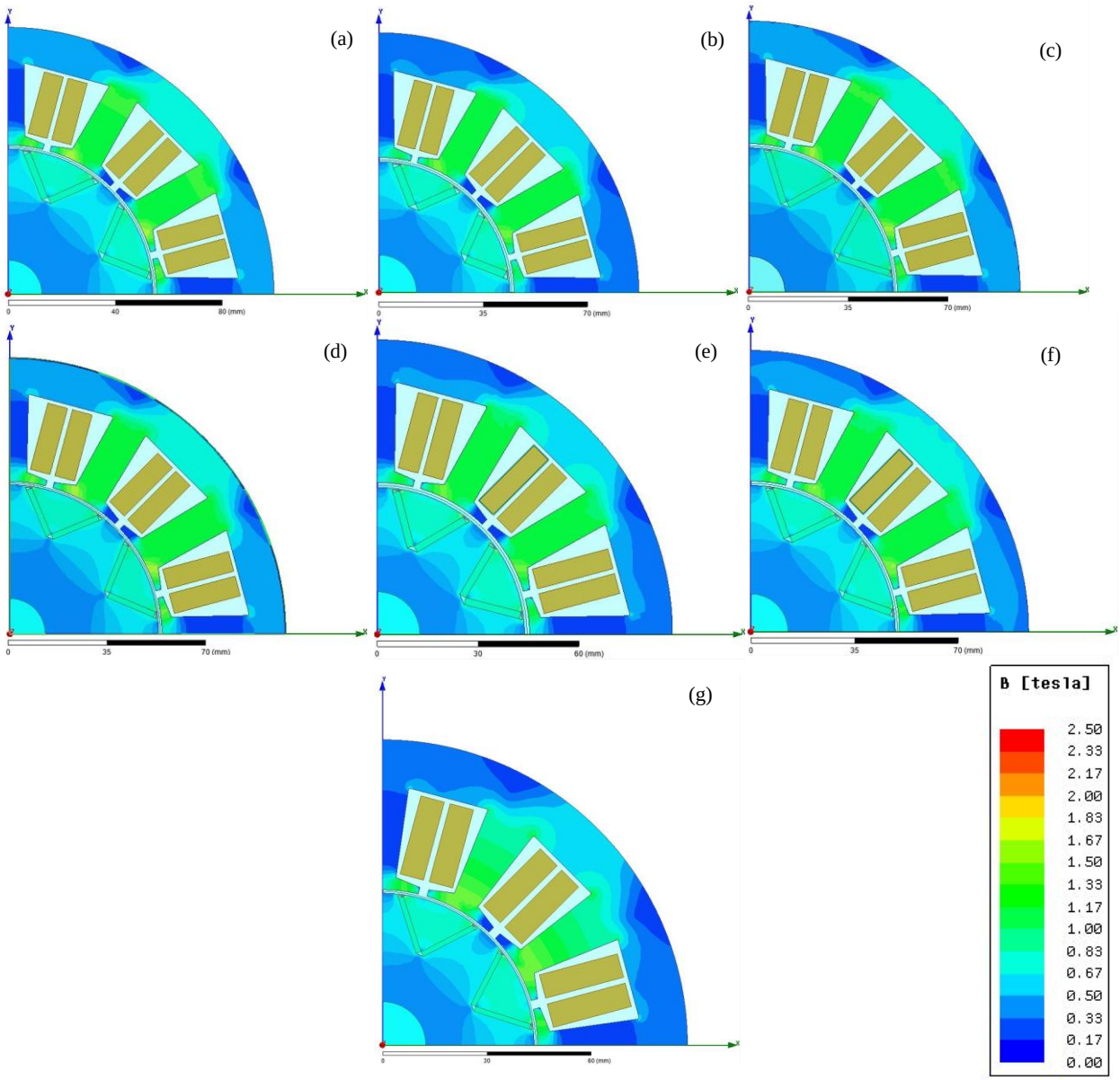

Figure 4.4 Flux density distribution for (a) Minimum-weight (GA), (b) Minimum-loss (GA), (c) Combined-objective (GA), (d) Minimum-weight (Simplex), (e) Minimum-loss (Simplex), (f) Combined-objective (Simplex), and (g) Preliminary machines.

Figure 4.4 confirms that the stators and rotors are not excessively saturated in any of the machines. The maximum flux density in the teeth is between 1.5 T to 1.6 T and is below the typical

saturation flux limit of M19 lamination, which is around 1.8 T. As such, acceptable iron losses are expected for all designed machines. Figure 4.5 represents the FEM results for the air-gap flux density distribution of the machines in one full electrical-cycle.

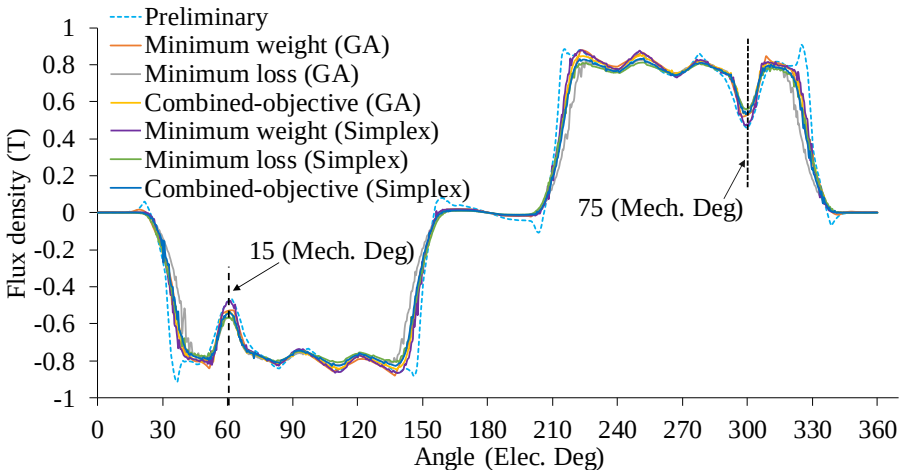

Figure 4.5 Air-gap flux density distribution profiles for the designed machines.

The two notches in the flux density profiles in Figure 4.5 are at the slot-opening locations at 15 and 75 degrees (mech.) and are due to the sudden change of reluctance by the increased air gap length in these areas. Since all optimized machines have the same magnet pitch, the air-gap flux densities are similar except for the preliminary design whose magnet width of 1.5 mm is far smaller than the magnet widths of all other designs. Accordingly, the above flux density profile for the preliminary design is more like a pure square wave compared to the other machines. The air-gap flux density harmonic spectra are analyzed and shown in Figure 4.6.

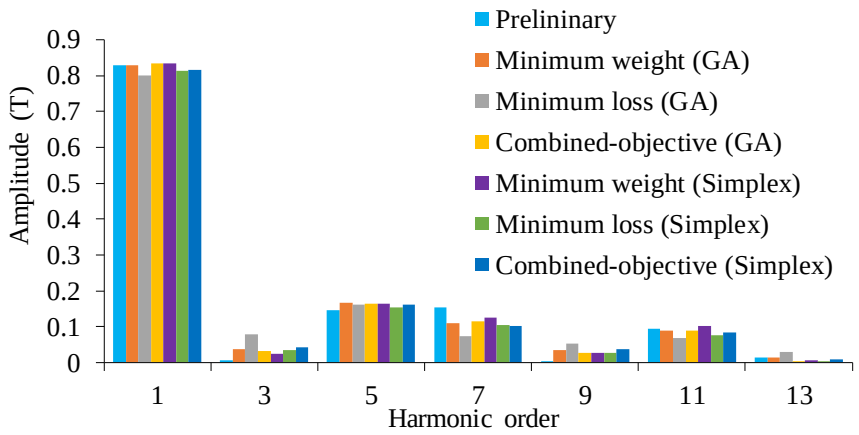

Figure 4.6 Air-gap flux density harmonic spectra.

According to Figure 4.6, triple-*n* harmonics are minimized in the air-gap flux density waveforms for all machines. In addition, the THD values of the air-gap flux densities are calculated based on (4.6).

$$B_{\mathrm{THD}} = \frac{\sqrt{\sum_{n=3}^{\infty} \left(\frac{4B_{\mathrm{m}} \sin(n\alpha)}{\sqrt{2} \times n\pi}\right)^2}}{4B_{\mathrm{m}} \sin(\alpha)/\sqrt{2}\pi} \times 100\% \tag{4.6}$$

Harmonic analysis of the air-gap flux density shows that the preliminary design has the highest air-gap flux density THD of 28%, while the Simplex minimum-loss design has the lowest THD of 25%. All other designs have THD values around 27%. The selected magnet pitch of 134 electrical degrees theoretically minimizes the THD of the air-gap flux density to 28%, which is confirmed by the FEM as well.

The back-EMF waveforms and their harmonic spectra are shown in Figure 4.7 and Figure 4.8, respectively. As seen, the Simplex minimum-weight design has the highest fundamental back-EMF of 164 V since it has the highest fundamental component air-gap flux density of 0.83 T and a relatively high number of turns per phase of 168 compared to the other designs. In addition, the fifth harmonics of the Simplex Algorithm designs are larger than those of the GA-based and

preliminary designs. According to the back-EMF THD analysis, the preliminary design shows the lowest THD of 6.2% due to the minimized fifth harmonic, and the Simplex combined-objective design has the highest THD of 14.5% due to the large fifth harmonic in its back-EMF waveform. GA combined-objective and minimum-weight designs show back-EMF THDs of 10%, while back-EMF THDs of 12.1% to 13.5% are seen for the other machines.

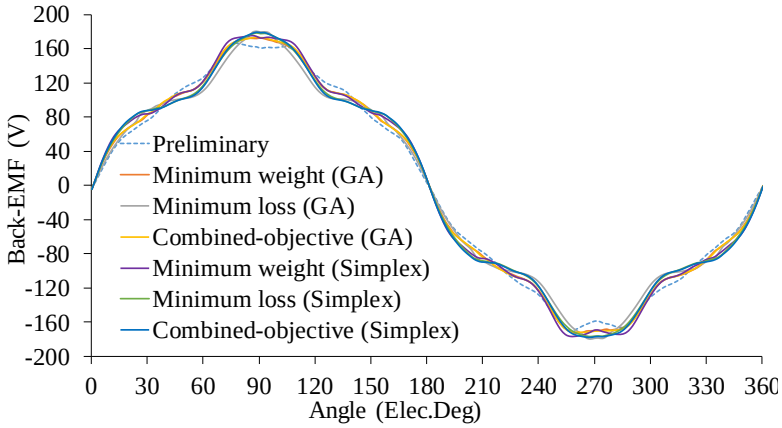

Figure 4.7 Back-EMF comparison at rated speed.

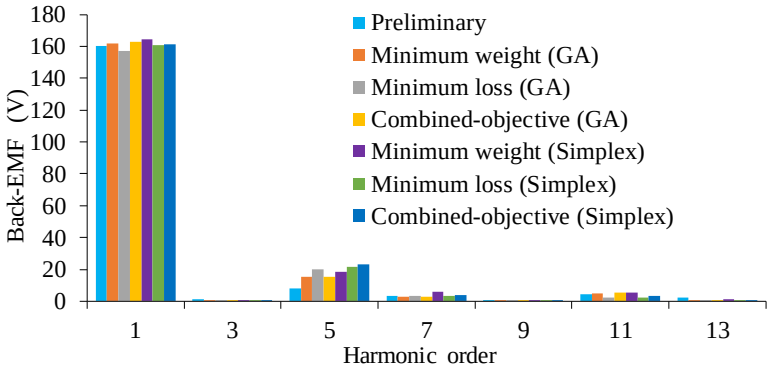

Figure 4.8 Back-EMF harmonic spectra comparison.

Inductance describes the ability of a coil to produce flux linkage and contributes to the speed of the machine by determining the characteristic current, which is the ratio of permanent magnet flux linkage over the d-axis inductance of the machine. In IPMSMs, the permanent magnets belong to the d-axis magnetic circuit, which increases the d-axis reluctance and causes the d-axis inductance to be smaller than that of the q-axis [11]. D-axis and q-axis inductances

contribute to the power density and speed range of the machine by determining the saliency ratio, which is the ratio of q-axis inductance to the d-axis inductance of the machine [91, 92]. Figure 4.9 shows the inductances and the saliency ratio comparison for the designed machines versus the current angle changes at the rated current.

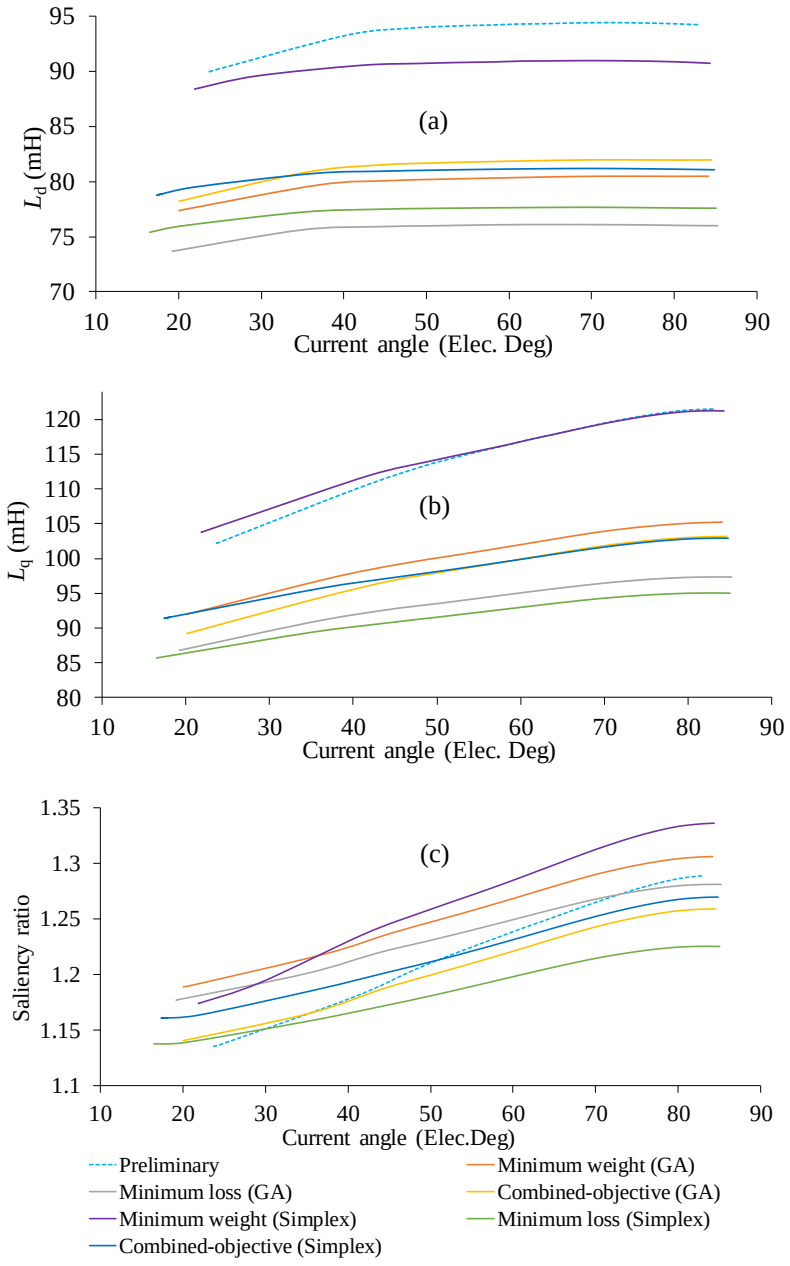

Figure 4.9 (a) d-axis and (b) q-axis inductances, (c) saliency ratio (L_q/L_d).

As seen, inductances are enhanced with the increment of the current angle. This phenomenon is due to the higher applied field-weakening current, which reduces the magnetization level in both d- and q-axis paths. In addition, the sensitivity of L_q to the current angle increment is higher than that of L_d. For example, 15-18 mH increment in L_q value is predicted versus current angle changes, while only 1-3 mH change for L_d value is expected for the same current angle change. The magnet width for the preliminary and minimum-weight Simplex designs are 1.5 mm, and 2 mm, respectively, while this parameter for all other machines is larger than 2.1 mm. This property causes less magnetized d- and q-axes and consequently larger L_d, and L_q. As seen in Figure 4.9 (c), the saliency ratio of all machines is larger than 1.12, and even reaches 1.33 for the minimum-weight simplex design.

Electric Machines Design Toolkit is used to verify the speed range, and the maximum developed power of the machines taking into account the current rating of (5A) and the maximum available voltage. The Maximum Torque per Ampere (MTPA) control method predicts the maximum developed torques of each design. The power-speed curves are shown in Figure 4.10.

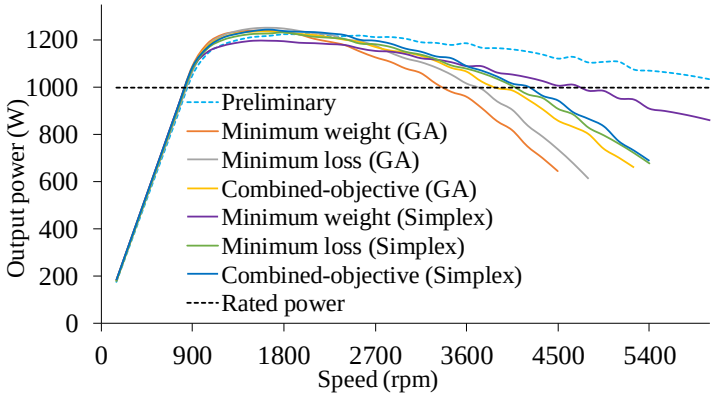

Figure 4.10 Output power versus speed comparison.

In an IPMSM, smaller characteristic current results in a wider speed range, while high saliency ratio increases the portion of reluctance torque in the average developed torque [93].

Therefore, a suitable compromise between these two parameters needs to be considered to propose a high torque density and wide speed range machine. According to Figure 4.10, the preliminary design has the widest speed range of 6000 rpm as it has the smallest characteristic current among all designs due to its comparatively large d-axis inductance. On the other hand, the GA minimum-weight design has the smallest speed range of 3300 rpm. Generally, the Simplex designs show wider speed ranges compared to their GA counterparts due to their relatively smaller characteristic currents. The machines' peak developed power are between 1200 W and 1250 W, with the GA minimum-loss design showing the highest peak power of 1250 W, and the Simplex minimum-weight design showing the lowest developed peak power of 1200 W.

Cogging torque is generated in an IPMSM due to the magnetic interaction between the rotor's permanent magnets and the teeth of the slotted stator. The circumferential component of the force attempts to maintain the alignment between the stator teeth and the magnet poles. These variations of the reluctance in the air gap along with the magnitude of the air gap flux linkages determine the magnitude of the cogging torque and must be lowered during the machine design process. This cogging torque reduction can be achieved with proper selection of slot pole combination, choice of double layer CW configuration for lowering down the air gap unwanted MMF components, and the proper shaping of the rotor poles or stator slots [18]. Cogging torque comparison for the designed machines is shown in Figure 4.11.

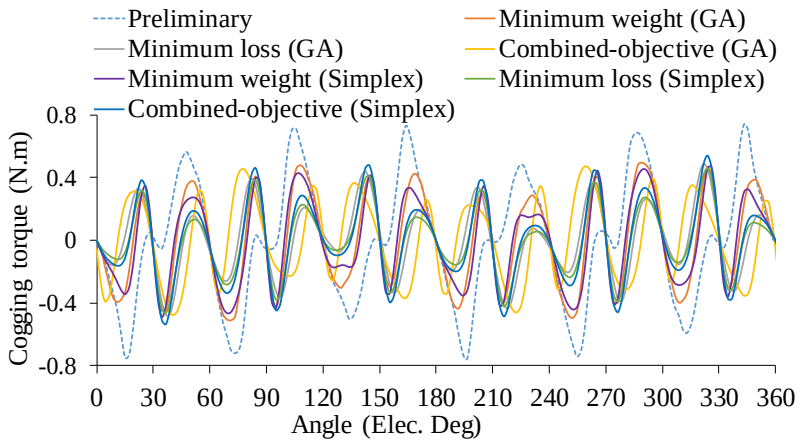

Figure 4.11 Cogging torque profile comparison for the designed machines.

According to Figure 4.11, the preliminary design shows the highest cogging torque peak of 0.75 N.m, while all the other optimized designs have cogging torque peak values below 0.5 N.m. The ratio of the slot opening over the rotor diameter is 0.29 for the preliminary design, while this value is in the range of 0.25 to 0.26 for the other machines. This relatively wider slot opening is the reason for the higher cogging torque in the preliminary design.

4.3.3 Loss and Efficiency Analysis using Finite Element Method

Mechanical losses are ignored in the simulation analysis, while the DC copper losses, iron losses, and AC copper losses due to the skin effect are considered for the efficiency assessment. The effectively utilized cross-section of the conductor in high frequency operating region is determined by the skin depth shown in (4.6) [24], where ρ is the resistivity and μ is the permeability of the conductor. Higher frequencies lead to smaller skin depth, reduced cross section for the conductor, and larger AC resistance for the winding. In this thesis, the AC copper losses associated with this phenomenon are called the solid losses (P_{solid}).

$$Skin\,depth = \sqrt{2\,\rho/(\omega\mu)} \tag{4.6}$$

The total losses (P_{loss}) of the machine in FEM are as follows;

$$P_{\text{loss}} = P_{\text{Cu}} + P_{\text{iron}} + P_{\text{solid}} \tag{4.7}$$

The profiles of iron, solid, and total losses versus speed are depicted in Figure 4.12 (a) to (c) respectively. It is worth noting that the DC copper losses (P_{cu}) are unchanged with the speed changes and are presented in the Table 4.4.

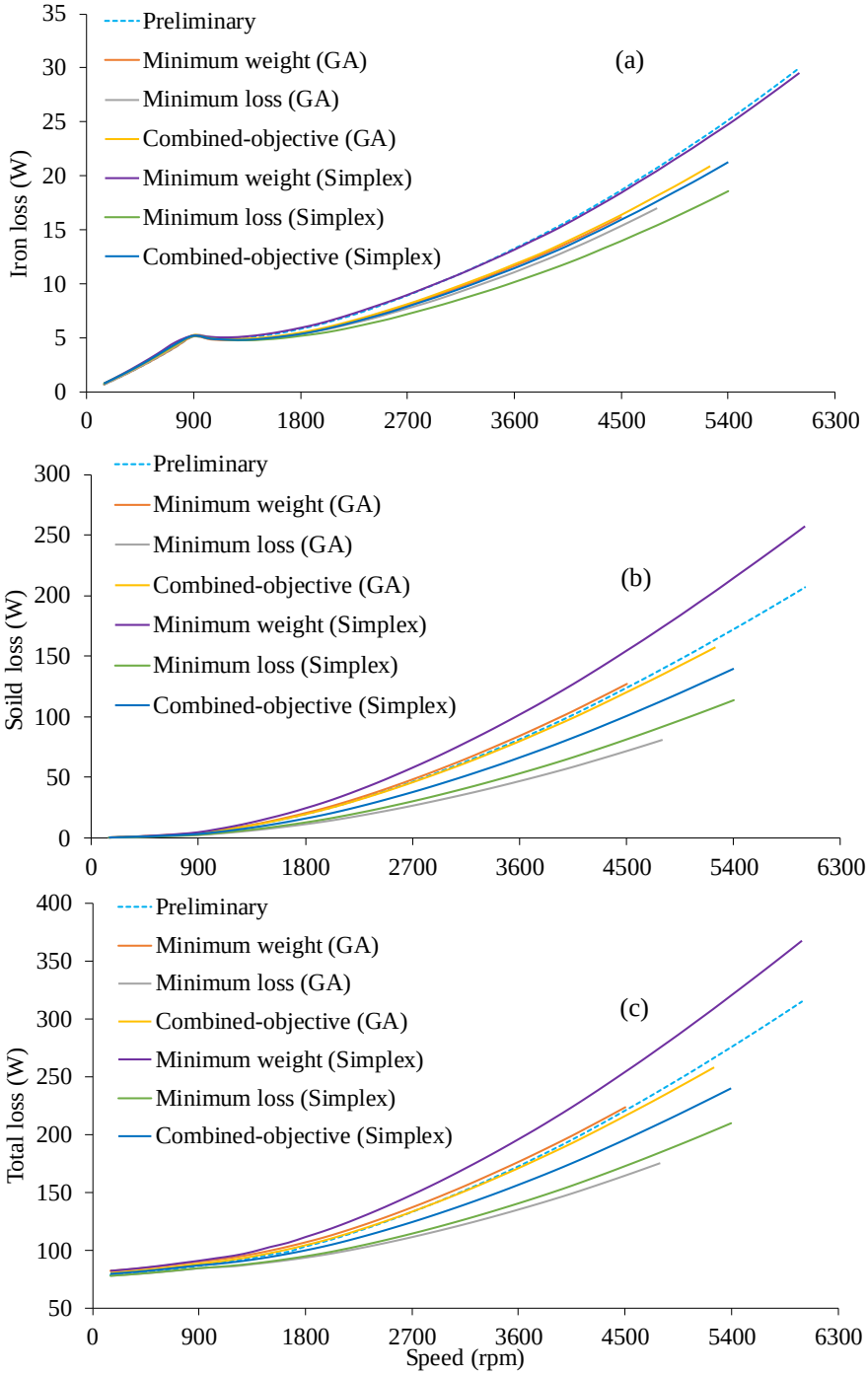

Figure 4.12 Evaluation of losses versus speeds using Finite element method (a) iron loss, (b) solid loss, and (c) total losses.

TABLE 4.4
DC COPPER LOSSES OF THE DESIGNED MACHINES

Design	DC Copper loss (W)
Preliminary	77.65
Minimum weight (GA)	81.18
Minimum loss (GA)	77.44
Combined-objective (GA)	79.14
Minimum weight (Simplex)	80.97
Minimum loss (Simplex)	77.51
Combined-objective (Simplex)	78.94

According to Figure 4.12, iron and solid losses are both functions of the speed, and the summation of these two losses has an ascending profile. That is why the total losses of the machines may vary from 80 W to even 320 W for the preliminary design in the speed range of 900 to 6000 rpm, while the Simplex-based minimum weight machine exhibits the highest total losses among all optimized designs from 82 W to 267 W in its speed range of 900 rpm to 4650 rpm.

According to Figure 4.12, the optimized minimum weight and preliminary designs show the highest total losses of up to 264 W and 320 W at their maximum possible speeds, respectively. Both the optimized minimum loss machines show lower total losses of up to 155 W at their maximum speeds because they have less copper in their phase windings and consequently 100 W less solid losses at higher speeds compared to their minimum weight counterparts. In addition, iron losses have a lower contribution to the total losses compared to the solid and copper losses.

The efficiencies of the compared machines are assessed using (2.37) and is plotted versus speed in Figure 4.13.

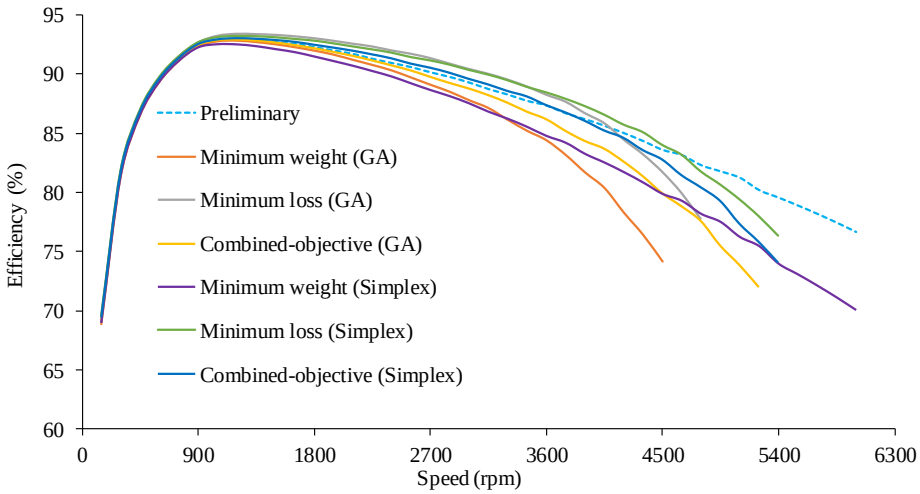

Figure 4.13 Efficiency versus speed profiles at maximum developed power.

According to Figure 4.13, the efficiencies reduce at higher speeds, and the preliminary design shows the highest efficiency at higher speeds due to its larger output developed power as evidenced by the simulation results shown in Figure 4.10. In addition, all of the compared machines show peak efficiencies above 92.50% at a speed of 1200 rpm. The efficiency of the optimized minimum loss machines is at least 1% to 2% higher than all other machines at the speeds above three times the base-speed.

4.4 Sensitivity Analysis

For sensitivity analysis, weight and efficiency values are re-calculated when variations are applied to L, δ, remnant flux density (B_r), P_{mw}, P_{mL}, end-winding length (C_{ea}), and D_o around their optimized values. (4.8) is used to calculate the sensitivity (S) of weight (W) and/or efficiency (η) (denoted as f) when perturbations (Δx_i) are applied to the selected design parameter, x_i*. Results are shown in Table 4.5.

$$S_i^f = \frac{f(x_1^*, \cdots, x_i^* + \Delta x_i, \cdots x_n^*) - f(x_i^*)}{\Delta x_i} \tag{4.8}$$

TABLE 4.5
WEIGHT AND EFFICIENCY SENSITIVITY ASSESSMENT

		L	δ	B_r	P_{mw}	P_{mL}	C_{ea}	D_o
Preliminary	W	0.86	≈0	0	≈0	≈0	0.14	2.12
	η	0.08	-0.07	0.14	0.07	0.07	-0.01	-0.06
Minimum weight (GA)	W	0.79	≈0	0	≈0	≈0	0.21	1.93
	η	0.11	-0.05	0.15	0.07	0.09	-0.02	-0.05
Minimum loss (GA)	W	0.86	≈0	0	≈0	≈0	0.14	2.12
	η	0.09	-0.05	0.14	0.06	0.09	-0.01	-0.06
Combined-objective (GA)	W	0.81	≈0	0	≈0	≈0	0.19	1.99
	η	0.1	-0.06	0.14	0.07	0.08	-0.01	-0.05
Minimum weight (Simplex)	W	0.8	≈0	0	≈0	≈0	0.19	1.95
	η	0.11	-0.06	0.15	0.08	0.09	-0.015	-0.05
Minimum loss (Simplex)	W	0.86	≈0	0	≈0	≈0	0.14	2.12
	η	0.09	-0.07	0.14	0.08	0.07	-0.013	-0.06
Combined-objective (Simplex)	W	0.83	≈0	0	≈0	≈0	0.17	2.03
	η	0.1	-0.05	0.14	0.07	0.09	-0.014	-0.05

According to Table 4.5, for a 1% increment in D_o, 1.93% to 2.12% increment is observed in the weights. The GA minimum-weight design shows the lowest weight sensitivity (1.93), while the preliminary and minimum-loss designs show the highest weight sensitivity (2.12) to D_o changes. For a 1% change in L, 0.79% to 0.86% increment is predicted for the total active weight of the machines. The GA minimum-weight design has the lowest weight sensitivity (0.79), while the highest weight sensitivity (0.86) is predicted for preliminary and minimum-loss designs for L changes. 0.14% to 0.19% increment in the total active weight of the machines is observed for a 1% increment in C_{ea}.

The efficiency is not overly sensitive to the selected parameters' variations. For example, for a 1% increment in B_r, only 0.14% to 0.15% variation is predicted for the efficiencies. A 1% increment in δ adversely contributes, by 0.05% to 0.07% change, to the efficiency of the machines.

A 1% increment in the magnet width and length has 0.06% to 0.09% positive contribution to increasing the efficiencies.

In addition to the sensitivity of the total active weight and efficiency to the tolerances of the design variables, the effect of λ variations on the optimized efficiency and total active weight is investigated and reported in Table 4.6. It is worth noting that Table 4.6 only shows the optimization results for the GA based globally optimized machine solution for brevity. According to Table 4.6, it is observed that by changing λ from small to large values an increasing emphasis is placed on the minimization of the total active weight. For example, the efficiency and the total active weight of the designed machine for λ=0 are 93.37% and 7.79 kg, respectively, while they are 92.86% and 7.27 kg when λ is equal to 14. Note that due to the fixed conductor gauge for all the designed machines the efficiency does not change drastically with λ. As the copper losses (Pcu) have the most significant effect on the total electromagnetic losses of the machine at the rated operating conditions, keeping the conductor size constant and using the same winding layout for all the designed machines may reduce the contribution of the loss minimization term in (4.3). In this case, the optimization algorithm attempts to minimize the resistance of the phase and the iron losses of the machine only by adjusting the number of turns and dimensions of the stator and rotor and without other factors such as conductor diameter or stator and rotor lamination type.

TABLE 4.6
VARIATIONS OF TOTAL ACTIVE WEIGHT AND EFFICIENCY WITH LAMBDA

λ	0	3	6	9	12	14
W (kg)	7.7904	7.7183	7.6736	7.4287	7.3426	7.3211
η (%)	93.37	93.15	92.99	92.92	92.90	92.88

4.5 Closing Remarks

GA and nonlinear Simplex Algorithm were used to optimize a V-shaped magnet IPMSM based upon three OFs. To predict the performance of the designed machines, finite-element based

electromagnetic analysis was carried and performances of the machines were compared in terms of their back-EMF voltage, cogging torque, saliency ratio, speed range, etc. It was shown that although the GA-based optimal designs have the best conformity to the defined OFs, the Simplex-based optimal designs may have superiority over the GA designs in terms of other characteristics such as speed range, which are not explicitly considered in the OFs. The comparative study provides suitable information to select a final design for fabrication not only from the OF viewpoint but also from other perspectives not directly included in the OFs. Sensitivity analysis was also carried out to check the effects of design variable changes on the weight and efficiency of the designed machines, and it was shown that the efficiency of the machines is much less sensitive to the parameter variations compared to the weight of the machines.

Chapter 5

Multimodal Design Optimization and Experimental Analysis

Contents

5.1 Introduction

In previous chapters, global and local optimizers were introduced and the dimensions and performances of a number of optimally designed IPMSMs were studied using different objective functions. In this chapter, a new multimodal optimization algorithm is applied for the optimization of the IPMSMs.

By using identical OFs defined in Chapter 4, the new multimodal optimization algorithm is used to provide all the possible global and local optimal results. Accordingly, a comparative study is conducted with the help of finite-element analysis using ANSYS-Maxwell software. This chapter will also present specifics about the constructed machine and its experimental validation.

5.2 Optimization Algorithm Setup

Identical independent variables along with the constraints discussed earlier are used to optimize the IPMSMs for the same OFs. The number of points in the initial mesh and the convergence criteria need to be selected carefully as they have significant effect the optimal

solutions found. In this thesis, these parameters are selected by trial and error after gaining experience with the algorithm to provide a balance between accuracy and computational burden.

In the program setup, the required equidistant sample points per design variable are selected to be eight in order to create the initial mesh for all designs. Additionally, the convergence in a local area is decided based upon the size of the hypercube encompassing the area.

Upon convergence, the algorithm finds eighteen optimal solutions (six optimal designs for each OF evolutions) by satisfying all of the given design constraints shown in Table 4.2. The procedure used to evaluate convergence in this program is as follows. Firstly, it identifies a local minimum area and then generates the points based upon the given density setting and estimates the OF values. The new estimated minimum value is compared with the existing minimum OF value and the algorithm calculates the error (Δe) in (5.1). Termination is decided when Δe is lower than a predetermined tolerance value.

$$Error\left(\Delta e\right) = \left| \, estimated \;\; minimum \;\; OF \;\; value - exsisting \;\; minimum \;\; OF \;\; value \, \right| \qquad (5.1)$$

Tables 5.1 to 5.3 show four optimal solutions for each of the three OFs: weight minimization (OF_1), electromagnetic losses minimization (OF_2), and simultaneous minimization of weight and electromagnetic loss (OF_3). All of them include one solution with the lowest OF (i.e., the global minimum), the preliminary design and the top three best-performing local minima.

TABLE 5.1
SPECIFICATIONS AND DIMENSIONS OF THE OPTIMALLY DESIGNED MACHINES FOR OF1

		Preliminary	Globally optimized	Locally optimized (Local minimum 1)	Locally optimized (Local minimum 2)	Locally optimized (Local minimum 3)
Weight	kg	8.3238	7.2773	7.5364	7.7746	7.8142
η_{Peak}	%	92.88	0.9212	0.9233	0.9234	0.9235
L	m	0.05	0.0331	0.0342	0.0353	0.0357
D_{rc}	m	0.0887	0.1086	0.1068	0.1056	0.1044
D_{ag}	m	0.0907	0.1115	0.1097	0.1080	0.1073
D_o	m	0.178	0.1996	0.2000	0.2000	0.1998
δ	m	0.0015	0.00145	0.00149	0.00122	0.00146
L_{sh}	m	0.0291	0.0294	0.0301	0.0307	0.0308
L_{tw}	m	0.0071	0.0117	0.0118	0.0124	0.0124
L_{yh}	m	0.0146	0.0147	0.0150	0.0153	0.0154
L_{isw}	m	0.0177	0.0185	0.0185	0.0174	0.0173
L_{osw}	m	0.0246	0.0329	0.0328	0.0319	0.0315
L_{so}	m	0.00265	0.0028	0.0028	0.0026	0.0026
P_{mw}	m	0.0015	0.0025	0.0021	0.0024	0.0022
P_{mL}	m	0.017	0.0180	0.0242	0.0183	0.0220
n_s	Turn	139	171	169	166	165

TABLE 5.2
SPECIFICATIONS AND DIMENSIONS OF OPTIMALLY DESIGNED MACHINES FOR OF2

		Preliminary	Globally optimized	Locally optimized (Local minimum 1)	Locally optimized (Local minimum 2)	Locally optimized (Local minimum 3)
Weight	kg	8.3238	7.7904	7.8770	7.8495	7.9287
η_{Peak}	%	92.88	93.3700	0.9269	0.9268	0.9268
L	m	0.05	0.0495	0.0493	0.0483	0.0496
D_{rc}	m	0.0887	0.0883	0.0885	0.0893	0.0882
D_{ag}	m	0.0907	0.0912	0.0913	0.0923	0.0910
D_o	m	0.178	0.1753	0.1768	0.1781	0.1769
δ	m	0.0015	0.00140	0.00141	0.00149	0.00141
L_{sh}	m	0.0291	0.0281	0.0285	0.0286	0.0286
L_{tw}	m	0.0071	0.0096	0.0095	0.0095	0.0095
L_{yh}	m	0.0146	0.0140	0.0142	0.0143	0.0143
L_{isw}	m	0.0177	0.0154	0.0160	0.0162	0.0159
L_{osw}	m	0.0246	0.0289	0.0292	0.0294	0.0291
L_{so}	m	0.00265	0.0023	0.0024	0.0024	0.0024
P_{mw}	m	0.0015	0.0025	0.0022	0.0022	0.0027
P_{mL}	m	0.017	0.0140	0.0180	0.0194	0.0156
n_s	Turn	139	140	140	142	140

TABLE 5.3
SPECIFICATIONS AND DIMENSIONS OF OPTIMALLY DESIGNED MACHINES FOR OF3

		Preliminary	Globally optimized	Locally optimized (Local minimum 1)	Locally optimized (Local minimum 2)	Locally optimized (Local minimum 3)
Weight	kg	8.3238	7.4287	7.7786	7.4628	7.6391
η_{Peak}	%	92.88	92.92	93.16	92.01	91.59
L	m	0.05	0.0369	0.0475	0.0371	0.420
D_{rc}	m	0.0887	0.1027	0.0906	0.1026	0.0971
D_{ag}	m	0.0907	0.1056	0.9310	0.1053	0.0990
D_o	m	0.178	0.193	0.1792	0.1943	0.1866
δ	m	0.0015	0.00145	0.00126	0.00137	0.00092
L_{sh}	m	0.0291	0.0292	0.0287	0.0297	0.0292
L_{tw}	m	0.0071	0.0114	0.0098	0.0111	0.0104
L_{yh}	m	0.0146	0.0146	0.0144	0.0148	0.0146
L_{isw}	m	0.0177	0.0173	0.0162	0.0181	0.0171
L_{osw}	m	0.0246	0.0318	0.0296	0.0319	0.0306
L_{so}	m	0.00265	0.0026	0.0024	0.0027	0.0026
P_{mw}	m	0.0015	0.0022	0.0022	0.0022	0.0023
P_{mL}	m	0.017	0.019	0.0150	0.018	0.0125
n_s	Turn	139	162	143	162	152

It is worth noting that the obtained global optima using the multimodal design optimization algorithm are similar to what was found by GAs in Chapter 4. This confirms that the multimodal algorithm is capable of finding the global optimum among its generated solutions. According to Table 5.1, the global optimum design saves at least 260 g of weight compared with its locally optimized design. In addition, the optimized machines save at least 500 g of weight compared with the preliminary design. However, the efficiency of the globally optimized machine is at least 0.21% less than the locally optimized machines. On the other hand, at least 0.68% efficiency gain, and 0.05 kg of weight reduction can be obtained with the selection of the globally optimized machine in Table 5.2; however, from an efficiency viewpoint, the preliminary design is better than locally optimize machines. Optimization results of OF_3 in Table 5.3 show that the globally optimized machine is at least 350 g lighter than a locally optimized machine while it is 0.24% less efficient than the highest efficient locally optimized machine 1.

With knowledge of these optimal solutions, the designer can embark on a detailed assessment of the optimally designed machines to compare them not only from the OF viewpoint but also from other aspects not directly included in the OF. In the next section, such a comparative assessment is performed on the preliminary design and two optimally designed machines, namely the globally optimized machine and the locally optimized machine corresponding to local minimum 1 in Table 5.3. Similar assessments can be performed for other local solutions, but are not shown here for brevity.

5.3 Comparative Assessment

5.3.1 Weights, Peak Efficiencies, and Sensitivity Analysis

According to the Table 5.3, the globally optimized machine has the shortest stack length of 36.9 mm, and largest stator outer diameter of 193 mm. The outer stator diameter and the stack length of locally optimal machine 1 lie between those of the preliminary and the globally optimized designs. The smallest weight of 7.428 kg belongs to the globally optimized design, which is 11% and 5.5% lighter than the preliminary design and locally optimal machine 1, respectively.

Copper losses are mainly a function of the conductor gauge which is fixed for all machines in this thesis (AWG 18). Copper losses vary between 77.65 W to 79.14 W and iron losses vary from 4.93 W to 5.33 W measured at the base speed. The number of turns per slot in locally optimized machine 1 is 11% less than the globally optimized machine due to its smaller air-gap. Also the stack length of the locally optimized machine 1 is 5% smaller than the preliminary design. Therefore, the locally optimized machine 1 has the highest peak efficiency, which is 0.24% and 0.28% higher than the globally optimized and preliminary designs, respectively.

It is seen that the weights of the designed machines are highly sensitive to their dimensions, while the efficiencies are not so. To investigate this issue, weight and efficiency values are re-

calculated when variations are applied to L, δ, B_r, P_{mw}, P_{mL}, end-winding length (C_{ea}), and D_o around their optimized values. Equation (4.8) is used to calculate the sensitivity (S) of weight (W) and/or efficiency (η) when perturbations (Δx_i) are applied to the design parameter, x_i*. Results are shown in Table 5.4.

TABLE 5.4
WEIGHT AND EFFICIENCY SENSITIVITIES FOR THE DESIGNED MACHINES

		L	δ	B_r	P_{mw}	P_{mL}	C_{ea}	D_o
Preliminary	W	0.86	≈0	0	≈0	≈0	0.14	2.12
	η	0.08	-0.07	0.14	0.07	0.07	-0.01	-0.06
Globally optimized	W	0.81	≈0	0	≈0	≈0	0.19	1.99
	η	0.1	-0.06	0.14	0.07	0.08	-0.01	-0.05
Local minimum 1	W	0.85	0	0	≈0	≈0	0.15	2.10
	η	0.09	-0.05	0.14	0.07	0.09	-0.01	-0.05

For a 1% increment in D_o, 1.99% to 2.12% increment is observed in the weights in globally optimized design and preliminary design respectively. The globally optimized design has the lowest weight sensitivity (0.81), while the highest weight sensitivity (0.86) is predicted for preliminary design for L changes. 0.14% to 0.19% increment in the total active weight of the machines is observed for a 1% increment in C_{ea}.

The efficiency is not highly sensitive to the selected parameters' variations if the conductor size is fixed for all machines (AWG 18 is used for all machines). For example, for a 1% increment in B_r, only 0.14% variation is predicted for the efficiencies. A 1% increment in δ adversely contributes, by 0.05% to 0.07% change in the efficiency of the machines. A 1% increment in the magnet width and length has 0.07% to 0.09% positive contribution to increasing the efficiencies.

5.3.2 Harmonic Analysis, Power Capabilities, and Cogging Torque Behaviour

The structures and the flux density distributions, at the rated power and speed for the three machines are shown in Figure 5.1.

According to the flux distributions shown in Figure 5.1, the flux density values of all the machines are below 1.7 T. This shows that the machines have low susceptibility to deep core saturation and high iron losses.

The air-gap flux density waveforms for the three designs are shown in Figure 5.2. Deep notches in the flux density waveform are predicted at the slot opening positions located at 60 and 300 electrical degrees due to the larger air-gap reluctance in these locations. Since the magnet width of the preliminary design is smaller than other two models, its air-gap flux density waveform is visibly different and more similar to a square waveform.

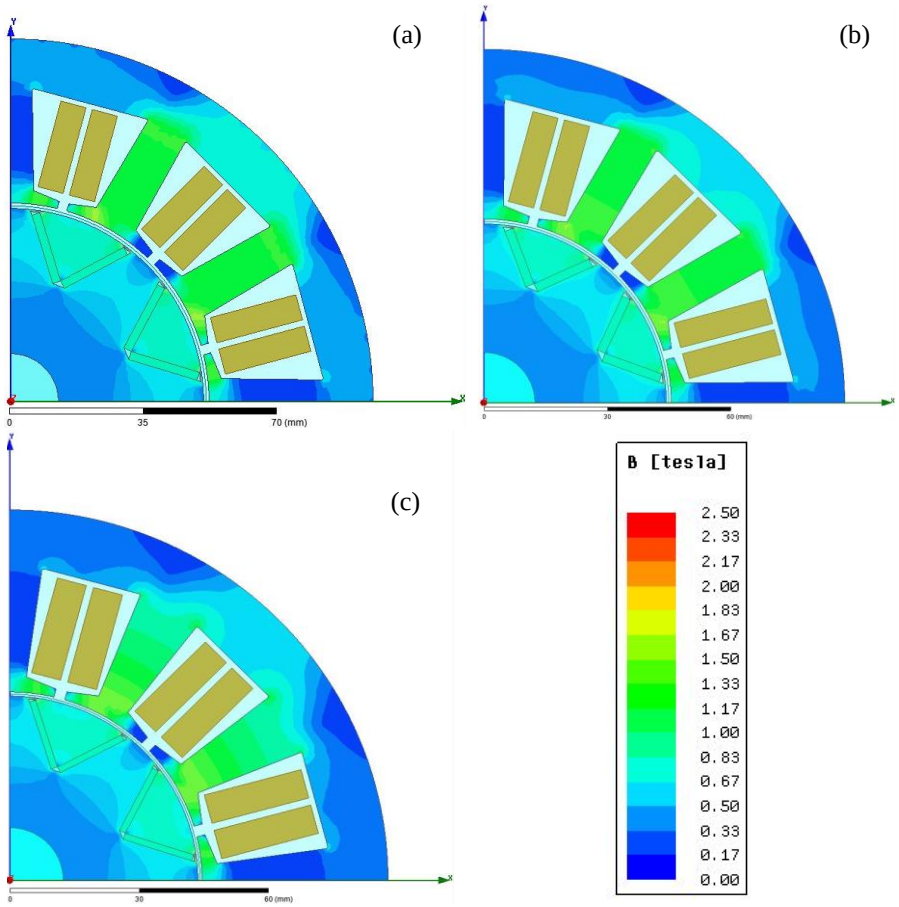

Figure 5.1 Structures and flux density distributions for (a) local minimum 1, (b) globally optimized, and (b) preliminary designs.

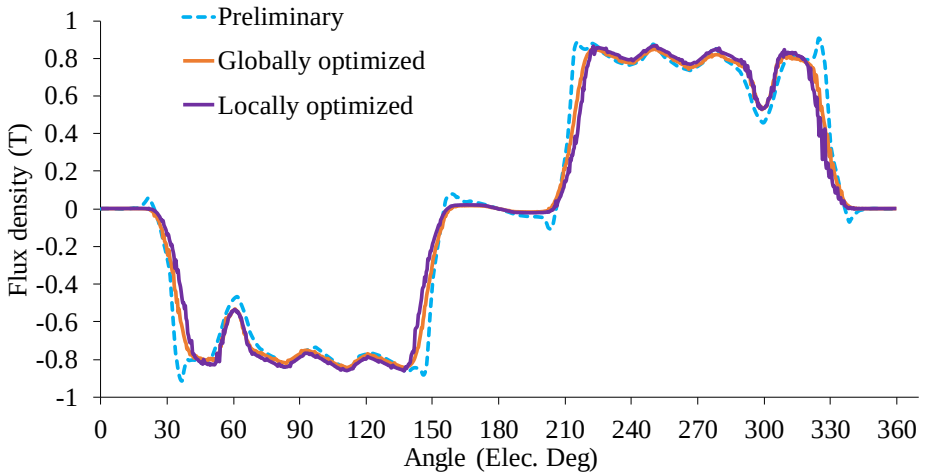

Figure 5.2 Air-gap flux density profiles for the designed machines.

The harmonic spectra of the air-gap flux density waveforms are shown in Figure 5.2. All machines have a fundamental air-gap flux density of around 0.81-0.82 T, while 3rd and 9th order harmonic components of all air-gap flux density waveforms are minimized. The preliminary design shows the lowest 3rd and 5th order harmonics in its air-gap flux density compared to the other two machines, while the locally optimized design shows the highest 3rd and 5th order harmonics. THDs are calculated in order to assess the harmonic contents of the air-gap flux density waveforms. Accordingly, the globally optimized and the preliminary designs have the lowest and the highest air-gap flux density THDs of 26% and 28.2%, respectively.

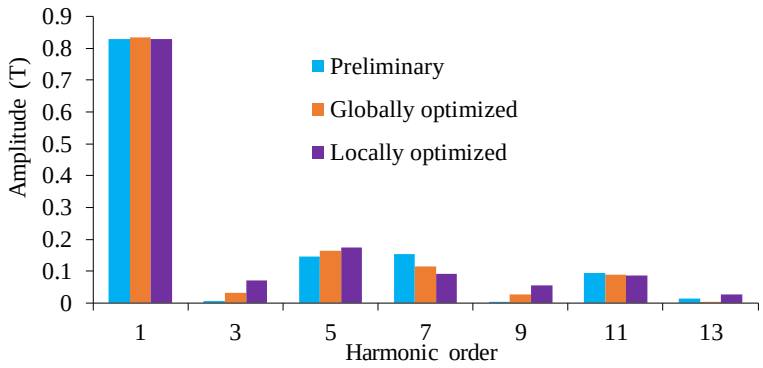

Figure 5.3 Air-gap flux density harmonic spectra

Verification of the speed range and the maximum developed power of the machines are analyzed utilizing the Electrical Machine Design Toolkit with Maximum Torque per Ampere control (MTPA) method. The obtained torque-speed curves are shown in Figure 5.4.

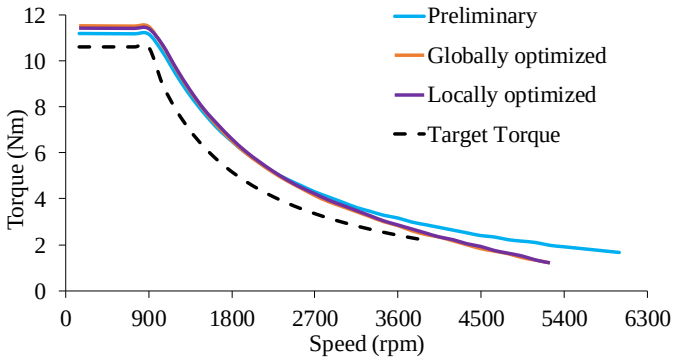

Figure 5.4 Torque versus speed characteristics

According to Figure 5.4, the developed torques of the machines are all above the target torque and the globally optimized machine has the highest developed torque compared to the other machines in this region. It is worth noting that developed torque maximization above the base speed and speed range widening are not within the focus of this research, as (i) accurate analytical formulation of the solid losses due to the skin and proximity effects is prohibitively difficult, and (ii) maximizing the speed range requires a new objective function to maximize the d-axis inductance and reluctance torque simultaneously. In addition, the globally optimized and the locally optimized designs have relatively similar torque-speed characteristics providing the rated power up to 3900 rpm (i.e., ~4 times base speed). For machines with the same permanent magnet flux linkage, the direct axis inductance (L_d) primarily determines the characteristic current. The d-axis inductance of the preliminary design is 95 mH, while that of the globally optimized and the locally optimized machines are 80 mH and 81 mH, respectively. This causes the preliminary design to have a wider speed range than other machines including locally optimized machine.

Cogging torque analysis is carried out for the three machines, and the profiles are depicted in Figure 5.5. The preliminary design has the highest peak cogging torque of 0.75 N.m, while its optimal counterparts both have a peak cogging torque of 0.5 N.m. As these machines have different stator inner diameters, the highest cogging torque can be expected in the machine having a higher ratio of the slot opening over the stator inner diameter. Hence preliminary design has the highest cogging torque with an ratio of 0.29 when this value is around 0.25 and 0.26 in global and locally optimized machine respectively.

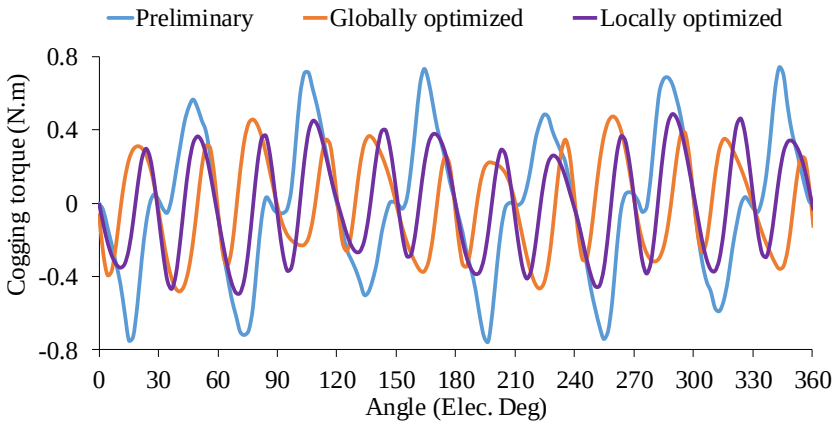

Figure 5.5 Cogging torque profile comparison for the designed machines.

5.3.3 Loss and Efficiency Analysis using FEM

In this section, mechanical losses are ignored in the simulation analysis, while the DC copper losses, iron losses, and solid losses here are considered for the efficiency assessment. After the calculations are done based on the equations presented in the section 4.3.3 for the losses of the machines, the profiles of iron, solid, and total losses versus speed are depicted in Figure 5.6. It is worth noting that the DC copper losses (P_{cu}) of the preliminary, globally optimized, and locally optimized machines are fixed versus speed and are equal to 77.65 W, 79.14 W, and 77.98 W, respectively. The efficiencies of the machines with the speed is shown in Figure 5.7.

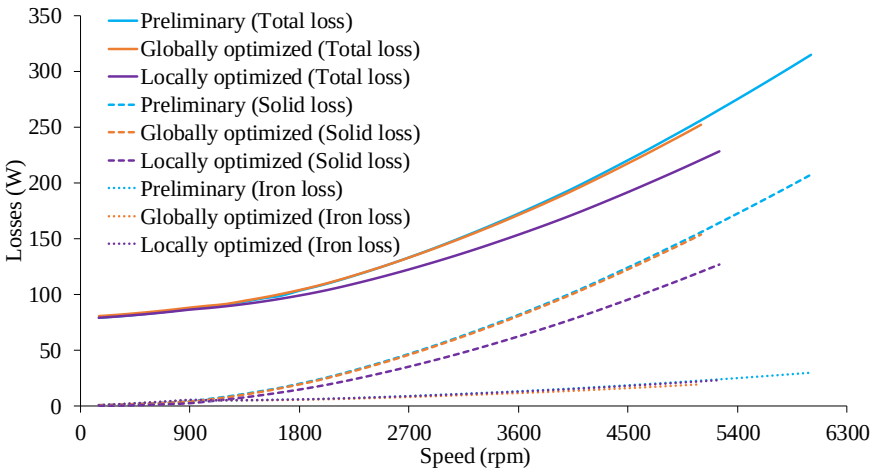

Figure 5.6 Loss versus speed evaluation using finite element method.

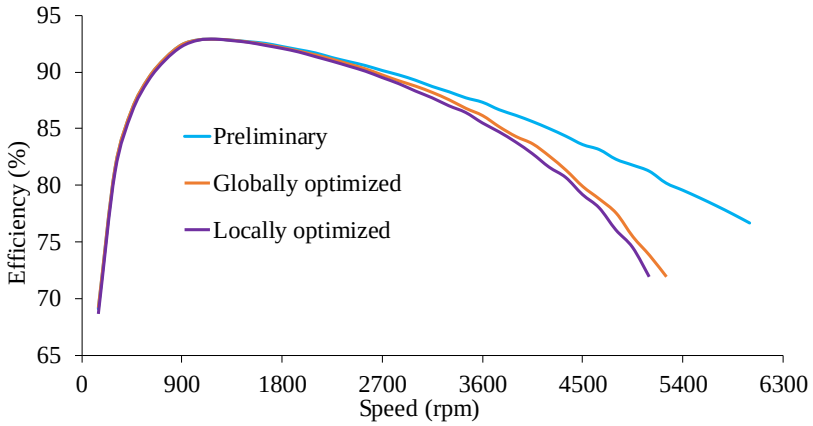

Figure 5.7 Efficiency versus speed profiles at maximum developed power.

According to Figure 5.6, the globally optimized and preliminary designs show the highest total losses of up to 250 W and 320 W at their maximum possible speeds, respectively. The locally optimized machine 1 shows lower total losses of up to 210 W at its maximum speed, because it has less copper in its phase winding and consequently 40 W less solid losses at higher speeds. In addition, iron losses have a lower contribution to the total losses compared to the solid and copper losses.

Following the same efficiencies patterns, locally optimized machine 1's efficiency is also reduced at the higher speeds. At speeds above three times the based speed, its efficiency is at least 1% to 2% lower than the globally optimized machine due to its higher torque/power density.

For experimental validations, the globally optimized machine is preferred to the preliminary design due to its 11% less weight and higher peak efficiency and is preferred to the locally optimized machine 1 because of its less sensitivity toward the parameter changes, wider speed range, lower air-gap flux density THD, smaller weight, and higher efficiency in high speed operating regions.

5.4 Computational Aspects of the Methods

The optimization problems in (4.1) to (4.3) ware solved on a 8-core (3.60 GHz Intel® Core-i7) machine with a 64-bit operating system and 8 GB of RAM. The optimization took nearly 220 s and the objective function was evaluated 2572834 times to complete and provided all local and global minima for each objective function. For comparison, computational time of GA is recorded as 22 s and for Simplex algorithm it was 6 s. Here the objective function is evaluated 1701000 and 540000 times to complete and provide global and local optimal results by GA and Simplex algorithms, respectively.

5.5 Experimental Validation

The globally optimized IPMSM is fabricated and its total active weight is compared with the simulations. In addition, the back-EMF voltage, losses, and efficiency are assessed to verify the accuracy of the design optimization technique and the expectations.

5.5.1 Machine Construction

The stator lamination, rotor lamination, and magnets with their detailed dimensions are shown in Figures 5.8 to 5.10, respectively.

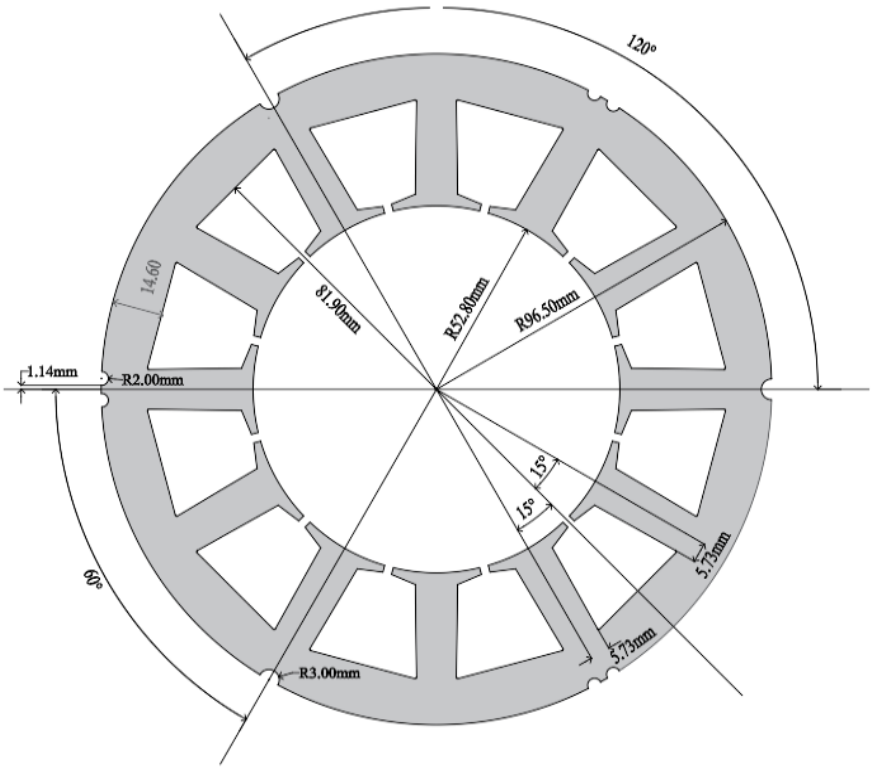

Figure 5.8 The stator lamination and its dimensions.

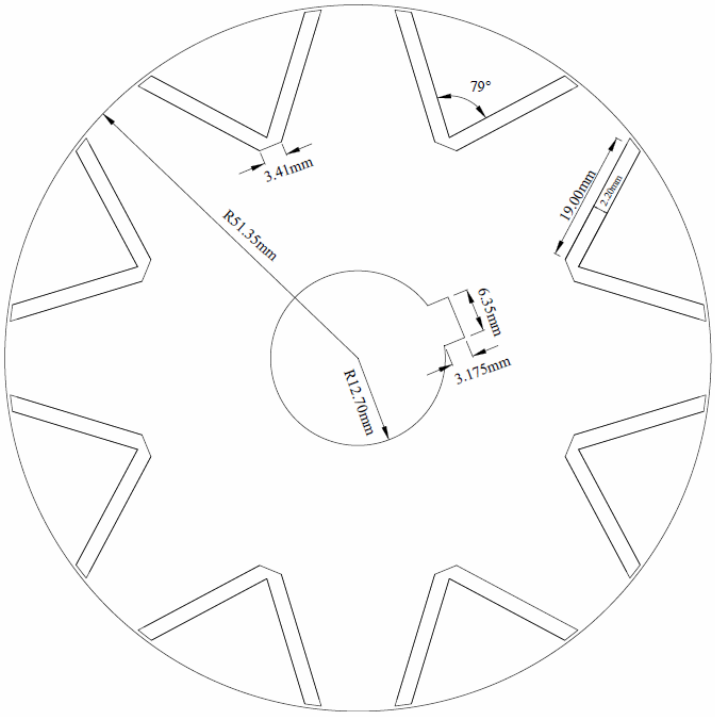

Figure 5.9 The Rotor lamination and its dimensions.

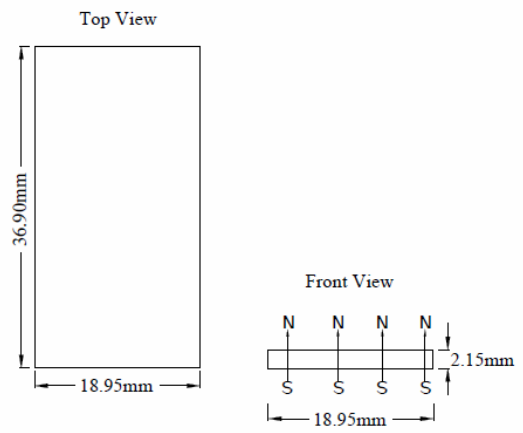

Figure 5.10: The utilized magnet and its dimensions.

Though all the dimensions in the above figure are equal to those used in the FEM simulations, machine fabrication needs minor modifications to the rotor and magnet dimensions. For instance, one key way hole is made on the rotor's shaft to physically fix the laminations. In addition, the length and the width of the drawn magnet are slightly smaller (reduced by 0.05 mm) than the simulated dimensions to allow the magnet to easily be inserted into the rotor without any severe pressure.

The 1095 spring steel, laser cut 29-gauge M19 laminations is used for the stator and rotor cores. The cut 29-gauge M19 stator and rotor laminations are shown in Figure 5.11.

(a) (b)

Figure 5.11: Actual laminations for a) stator, b) rotor

102 stator and rotor laminations are aligned and pressed to build the 3.69 cm stack. The constructed stator and rotor assemblies of the machine are shown in Figure 5.12.

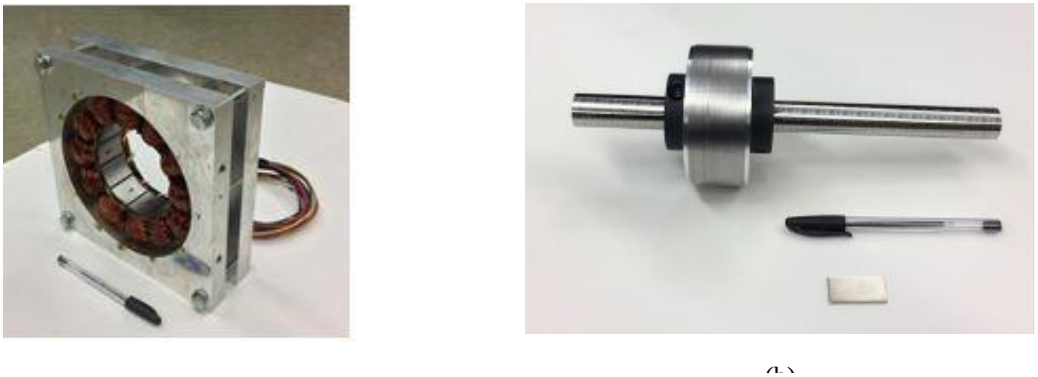

Figure 5.12 Constructed machine: (a) stator, (b) rotor and a magnet.

Figure 5.13, Figure 5.14 (a), and Figure 5. 14 (b) show the winding arrangement of the three phase 12 slot-8 pole IPMSM, the actual wound stator structure, and the constructed machine respectively.

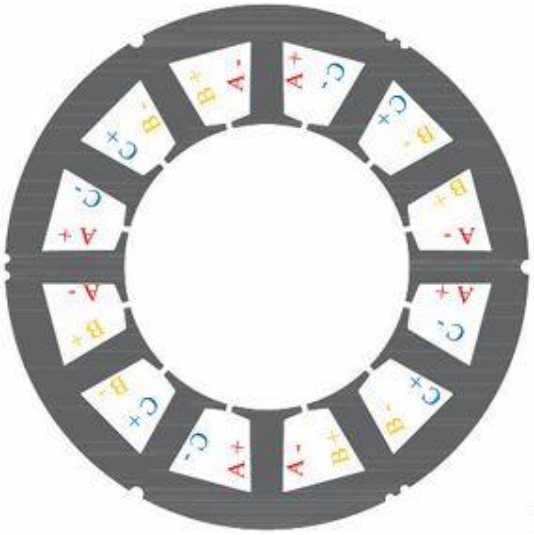

Figure 5.13 Winding arrangement for the three phase 12 lost 8 poles IPMSM

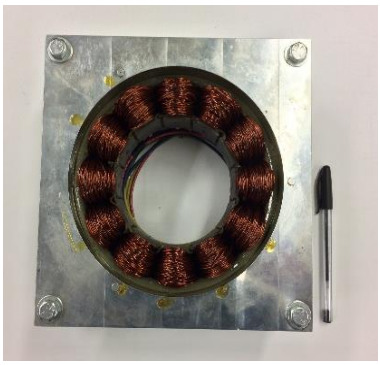

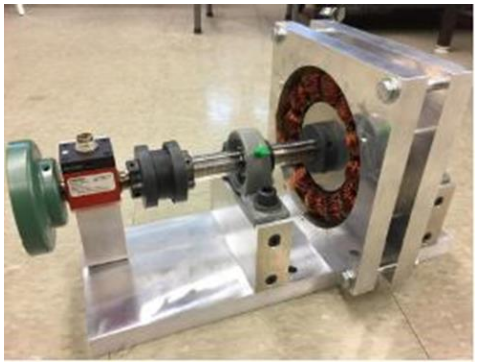

(b)

Fig. 5.14 (a) The actual wound stator, (b) constructed machine ready for the tests

5.5.2 Comparison of the Masses of the Simulated and Built Machines

The masses of different components of the simulated and constructed globally optimized machine are listed in Table 5.5. The built machine is 0.367 (kg) heavier than the simulated one due to the presence of the end winding in the built machine.

TABLE 5.5
WEIGHT COMPARISON FOR THE GLOBALLY OPTIMIZED MACHINE

	Stator	**Rotor**	**Copper**	**Magnets**	**Total**
Simulated (kg)	3.367	1.891	1.988	0.182	7.428
Constructed (kg)	3.360	1.883	2.376	0.176	7.795

5.5.3 Test Rig and Experimental Results

To assess the performance of the built machine, the test rig shown in Figure 5.15 is prepared. A 2-kW, 4-quadrant dynamometer is used for loading the IPMSM in motor mode and serves as a prime mover in generator mode to evaluate the machine's back-EMF. A 3-hp ABB PWM converter is used to control the speed and voltage of the machine and a 20-N.m, FUTEK torque transducer measures the developed torque.

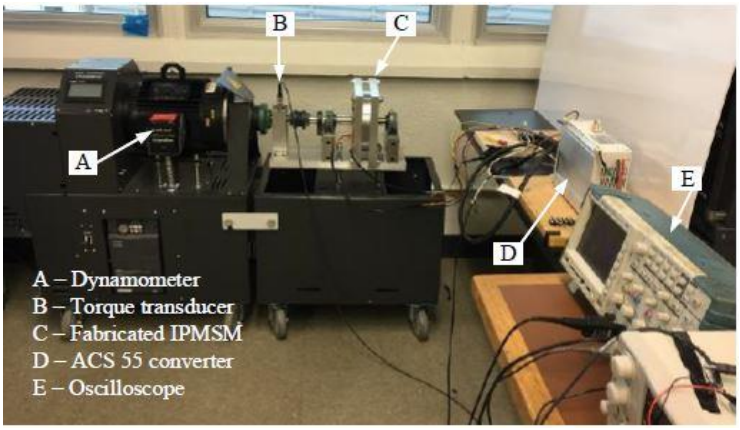

Figure 5.15 Complete experimental setup.

The back-EMF waveform is measured at 900 rpm and is compared with the simulation in Figure 5.16. The peaks of the measured and simulated back-EMF waveforms are exactly same and are equal to 160 V. The THD of the simulated back-EMF voltage is 10.2% and is 14.4% in the experimental assessment. Non-ideal magnetic properties of the actual laminations and magnetization direction in the magnets are the main reasons for slightly higher harmonic contents in the built machine.

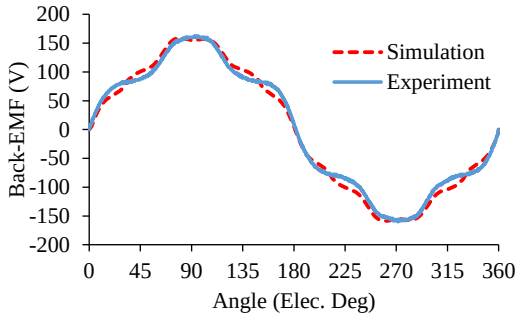

Figure 5.16 Simulated and measured back-EMF waveforms (at 900 rpm).

The fabricated IPMSM is loaded from half load to full load (10.6 N.m) at its base speed, and its losses and efficiencies (see (5.2)) are compared with the simulation results, the results are as shown in Figures 5.17 and 5.18, respectively.

$$\eta(\%) = \tau_{\text{load}}\ \omega_{\text{m}} / P_{\text{in}} \times 100 \tag{5.2}$$

where τ_{load} is the developed torque of the machine in (N.m), ω_m is the mechanical speed in (rad/s), and P_{in} is the input power in (W) using the measured phase voltage and current.

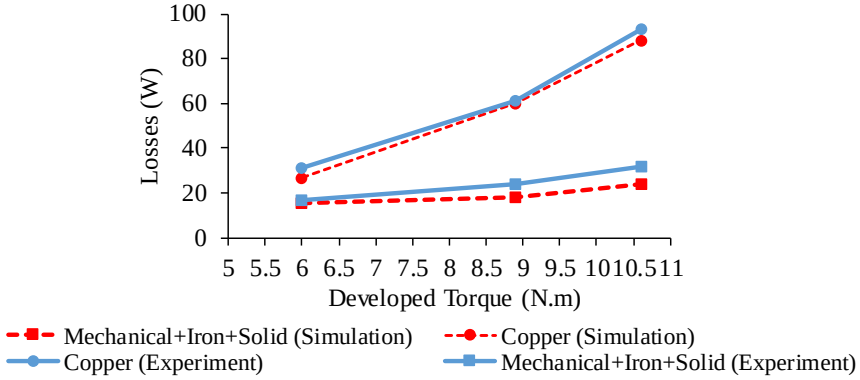

Figure 5.17 Loss evaluation in simulations and experiments.

According to Figure 5.18, the copper losses in simulations and experiments both show ascending profiles versus load increments as higher currents are drawn. Copper losses vary from 30 W to 93 W in experiments, and from 26 W to 89 W in simulations. The main reason for this discrepancy is the relatively larger required current for the same load in the experiments due to having higher harmonic losses in the built machine especially in the higher developed torques, and also the presence of the end winding in the built machine which is neglected in 2D-FEM simulations. The machine is tested in no load condition and the mechanical loss equal to 10 W is observed in the base speed. Copper losses are subtracted from the total losses to obtain the summation of the mechanical, iron, and solid losses in the experiments. The observed 10 W mechanical loss is taken into account for the loss analysis in simulations, and the iron and solid losses are obtained using 2D-FEM in the base speed and various load levels.

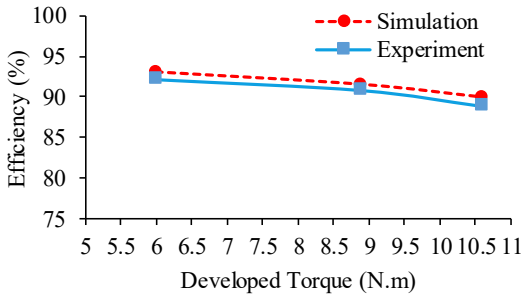

Figure 5.18 Efficiency comparison between simulations and experiments

According to Figure 5.18, a promising agreement between the efficiencies in simulations and experimental analysis is seen, which confirms the accuracy of the optimization steps and the reliability of the obtained optimal design for the desired operation. 0.7% to 1% difference is seen between the simulated and experimental efficiencies which make sense when manufacturing tolerances, non-ideal magnetization of the laminations, and neglected flux distribution in the z-axis direction in the 2D-FEM are all taken into consideration.

5.6 Closing Remarks

A V-Shaped magnet IPMSM was optimally designed using multimodal design optimization technique to fulfill three different OFs. The multimodal optimization technique was fully capable to find all the local and global minima for each defined OF. The globally optimized machine was exactly identical to the one found by GA in the previous chapter verifying the effectiveness of the multimodal approach to come up with the global solution among its generated solutions. The predicted performance of the combined-objective based globally optimized design was compared with the preliminary and locally optimized designs to show the merits and disadvantages of each design. The globally optimized machine was selected for the fabrication, and the experimental performance of this machine was compared with the simulation analysis to prove the accuracy and the reliability of the optimized machine. Only 1% to 1.6% error between

the simulated and experimental efficiencies was observed due to the manufacturing tolerances confirming a close agreement between the expectations and real tests.

Chapter 6

Contributions, Conclusions, and Recommendations for Future Work

Contents

The main concluding remarks, contributions and some suggestions for future work are described in this chapter.

6.1 Conclusions

The main objective of this thesis was to optimally design a concentrated winding V-shaped magnet IPMSM by means of various optimization techniques while considering different objective functions (OFs). Comparative studies and sensitivity analysis on the predicted operating characteristics of the designed machines were conducted. The advantages and disadvantages of each design were clarified not only from the OF evaluation perspective but also from other viewpoints not directly included in the defined OFs. Initially, a local optimizer (nonlinear Simplex) and a global optimizer (Genetic Algorithms) were separately used to determine the dimensions of each optimized machine based on three distinctive OFs: (i) minimize the weight, (ii) minimize the electromagnetic losses, and (iii) minimize the losses and weight in a combined-objective solution.

The second objective of this thesis was to establish a multimodal optimization algorithm, which could find all the local and global minima of a defined OF at the same time. The multimodal

algorithm enables the user to have access to all alternative designs in an affordable time compared to the sophisticated FEM-based motor design optimization techniques. In order to verify the simulation predictions, a prototype of the optimized machine was fabricated. The experimental results demonstrated that the constructed machine performs closely to expectations confirming the accuracy, effectiveness, and reliability of the design optimization steps and simulation analysis.

6.2 Contributions

In Chapter 2 conventional electrical and magnetic loading principles taking into account the voltage and current limitations for the desired output power, efficiency, and power factor were used to obtain the dimensions of a machine. The obtained dimensions of this designed machine were not based on any optimization algorithm and could only satisfy the basic requirements within the desired outputs and defined dimensions. The design of this machine was preliminary and its performance was compared with the other machines in the next chapters of the thesis.

Chapter 3 introduced the global, local, and a multi-modal optimization algorithm and showed how these optimization techniques work and how they can be used to find the optimized dimensions of the machines in various defined OFs.

Chapter 4 showed that although GA-based optimal designs performed best to the defined OFs. Furthermore, the Simplex-based optimal designs were superior to the GA designs in terms of other characteristics not explicitly considered in the OFs. This comparative study alongside with the sensitivity analysis provided comprehensive insight into the process of selecting the best overall machine for the fabrication purposes.

According to Chapter 5, the developed multimodal optimization algorithm enabled comparative assessment of multiple optimal solutions, and due to its advantages over its other counterparts, it was selected for the experimental analysis. It is worth noting that the obtained

globally optimized machines found by the multimodal optimization technique were identical to the ones found by the GA. This point confirms the capability of the multimodal optimization technique to include the globally optimized designs among its other generated solutions. The experimental back-EMF, losses, and efficiency demonstrated that the constructed machine performs closely similar to the expectations verifying the reliability of the design optimization steps.

6.2.1 Publications

This study led to two research publications at reputable international conferences; one journal publication is under review at the time of writing this thesis.

1. B. D. Guruwatta Vidanalage, M. S. Toulabi, and S. Filizadeh, "A Comparative Study of Optimally Designed V-Shaped Magnet IPM Synchronous Motors," in proc. *IEEE International Conference on Electrical Machines and Systems (ICEMS)*, pp 1-6, Aug. 2017.

2. B. D. Guruwatta Vidanalage, M. S. Toulabi, and S. Filizadeh, "Electromagnetic Design Optimization and Sensitivity Analysis for IPM Synchronous Motors," in proc. *IEEE International Conf. on Industrial Technology (ICIT)*, pp. 288-293, Mar. 2017.

3. B. D. Guruwatta Vidanalage, M. S. Toulabi, and S. Filizadeh, "Multimodal Design Optimization of V-Shaped Magnet IPM Synchronous Machines," *IEEE Trans. on Energy Conversion*, revision submitted.

6.3 Suggestions for Future Work

This study can be improved in several ways. In the simulation analysis, it was assumed that the windings of the machine are not exposed to free air, and the current density of 4 A/mm^2 was adjusted during the optimization procedure accordingly. To overcome possible thermal issues, and low-efficiency problems in the experimental steps, the machine was not placed in a closed housing and the windings were exposed to free air movement. This provision supported a higher-efficiency performance with no thermal problem during experimental analysis even in full load operation. However, in order to accurately predict the thermal behavior of the machine at various load levels and precisely select the conductor gauge, building a detailed thermal-resistance circuit is recommended. This issue may cause to select a lower cross-section area conductor for the designed machine leading a lower total active weight but increase of copper losses due to the conductor resistance increment.

Another area for further inquiry is losses. Thinner laminations with lower loss density can help the designed machine to have lower losses and higher efficiency. In addition, having more accurate loss data for the laminations can increase the reliability of the simulation results.

If the conductor sizes and winding arrangement are kept fixed for all designs, the optimized efficiency of the machines does not change extensively. Accordingly, considering the other slot pole combinations, winding arrangements, and conductor sizes are recommended especially for the combined-objective optimization.

References

[1] I. Boldea, "Electric Generators and Motors: an overview," *CES Trans. Electrical Machines and Systems,* vol. 1, no. 1, Mar. 2017.

[2] M. A. Nicolaescu, "Rotary Electrical Motors used in Medical Industry Relevant Design Considerations and Actual Advances," in *Proc. Int. Conf. and Exposition on Electrical and Power Eng. (EPE),* pp. 664-667, Oct. 2012.

[3] H. Saavedra, L. Romeral and J. R. Riba, "Optimal Design of a Three-Phase AFPM for in-Wheel Electrical Traction," in *Proc. IEEE Int. Electric Vehicle Conf. (IEVC),* pp. 1-7, Dec. 2014.

[4] G. Snitchler, B. Gamble and S. S. Kalsi, "The Performance of a 5 MW High Temperature Superconductor Ship Propulsion Motor," *IEEE Trans. Applied Superconductivity,* vol. 15, issue. 2, pp. 2206-2209, Jun. 2005.

[5] L. Chong, "Design of an Interior Permanent Magnet Machine with Concentrated Windings for Field Weakening Applications," Ph.D. thesis, *The University of New South Wales,* Aug. 2011.

[6] Electric motors energy efficiency reference guide [Online], Available: www.saskpower.com.

[7] J. Parrish, S. Moll and R. C. Schaefer, "Synchronous versus Induction Motors: Plant Efficiency benefits resulting from the use of Synchronous Motors," *IEEE Ind. Appli. Magazine,* vol. 12, issue. 2, pp. 61-70, Feb. 2006.

[8] J. M. Mun, G. J. Park and S. Seo, “Design Characteristics of IPMSM with Wide Constant Power Speed Range for EV Traction,” *IEEE Trans. Magn.*, vol. 53, issue. 6, Jun. 2017.

[9] N. Bianchi, E. Fornasiero, M. Ferrari and M. Castiello, “Experimental Comparison of PM-Assisted Synchronous Reluctance Motors,” *IEEE Trans. Ind. Appl.*, vol. 52, issue. 1, pp. 163-171, Jan.-Feb. 2016.

[10] J. *Pyrh¨*onen, T. Jokinen and V. Hrabovcov´a “*Design of Rotating Electrical Machines*”, Great Britain: John Wiley & Sons, Ltd., 2008.

[11] R. Dutta, “A Segmented Interior Permanent Magnet Synchronous Machine with Wide Field-Weakening Range,” Ph.D. thesis, *The University of New South Wales*, Aug. 2007.

[12] H. Liu, Z. Gao, W. Wu, L. Chow and T. Wu, “Design of a High-Efficiency Permanent Magnet Synchronous Motor and Inverter System,” in *Proc. IEEE Ind. Electronics Society (IECON)*, pp. 4996-5001, Nov. 2015.

[13] J. H. Seo, S. Y. Kwak, S. Y. Jung, C. G. Lee, T. K. Chung and H. K. Jung, “A Research on Iron Loss of IPMSM with a Fractional Number of Slot Per Pole,” *IEEE Trans. Magn.*, vol. 45, no. 3, pp. 1824-1827, Mar. 2009.

[14] M. Dubey, S. Sharma and R. Saxena, “Single stage PV system based Direct Torque Controlled PMSM drive for pump load application,” in *Proc. IEEE Int. Conf. on Power Electronics, Drives and Energy Systems (PEDES)*, pp. 1-5, Dec. 2016.

[15] W. Zhao, T. A. Lipo, and B. Kwon, “Dual-Stator Two Phase Permanent Magnet Machines with Phase-Group Concentrated-Coil Windings for Torque Enhancement,” *IEEE Trans. Magn.*, vol. 51, no. 11, Art. ID 8112404, Nov. 2015.

[16] T. Genda , I. R. Kartono, M. Yoneda and H. Dohmeki, " Basic performance of Inset type PMSM," in *Proc. Int. Conf. on Electrical Machines (ICEM),* pp. 1-6, Sep. 2008.

[17] X. Liu, H. Chen, J. Zhao, and A. Belahcen, "Research on the Performances and Parameters of Interior PMSM used for Electric Vehicles," *IEEE Trans. Ind. Electron*., vol. 63, no. 6, pp. 3533-3545, Jun. 2016.

[18] L. Chong, R. Dutta and M. F. Rahman, "A Comparative Study of Rotor Losses in an IPM with Single and Double Layer Concentrated Windings", in *Proc. Int. Conf. on Electrical Machines and Systems (ICEMS),* pp. 942-946, Oct. 2010.

[19] L. Chong, R. Dutta and M.F. Rahman, "Application of Concentrated Windings in Interior Permanent Magnet Machine," in proc. *Australasian Universities Power Eng. Conf.,* pp. 1-5, Dec. 2007.

[20] L. Chong, R. Dutta, H. Lovatt, N. Q. Dai and M. F. Rahman, "Comparison of Concentrated and Distributed Windings in an IPM Machine for Field Weakening Applications*",* in *Proc. Australasian Universities Power Eng. Conf.,* pp. 1-5, Dec. 2010.

[21] L. Chong, R. Dutta, M. F. Rahman and H. Lovatt "Experimental verification of Rotor Losses in a Concentrated Wound IPM Machine with V-Shaped magnets," in *Proc. IEEE Int. Electric Machines & Drives Conf. (IEMDC),* pp. 1-5, Dec 2010.

[22] R. Dutta, L. Chong and M. F. Rahman, "Analysis of CPSR in Motoring and Generating modes of an IPM motor," in *Proc. IEEE Int. Electric Machines & Drives Conf. (IEMDC),* pp. 1474-1479, May 2011.

[23] L. Chong, R. Dutta and M.F. Rahman, "Design and mechanical consideration of an IPM Machine with Concentrated Windings," in *Proc. Australasian Universities Power Eng. Conference*, pp. 1-6, Sept. 2009.

[24] M. S. Toulabi, J. Salmon and A. M. Knight, "Concentrated Winding IPM Synchronous Motor Design for Wide Field Weakening Applications," *IEEE Trans. Ind. Appl.*, vol. 53, no. 3, May-Jun. 2017.

[25] M. S. Toulabi, J. Salmon and A. M. Knight, "Design and Performance Assessment for the V Shaped Magnet IPM Synchronous Motor," in *Proc. IEEE Int. Electric Machines & Drives Conf. (IEMDC)*, pp. 214-219, May 2015.

[26] N. Bracikowski, M. Hecquet, P. Brochet and S. V. Shirinskii, "Multiphysics Modeling of a Permanent Magnet Synchronous Machine by Using Lumped Models," *IEEE Trans. Ind. Electron*, vol. 59, issue. 6, pp. 2426-2437, Jun. 2012.

[27] A. Hemeida and P. Sergeant, "Analytical Modeling of Surface PMSM Using a Combined Solution of Maxwells Equations and Magnetic Equivalent Circuit," *IEEE Trans. Magn.*, vol. 50, issue. 12, Art. ID 14810501, Dec. 2014.

[28] R. Dutta and M.F. Rahman, "An Investigation of a Segmented Rotor Interior Permanent Magnet (IPM) Machine for Field Weakening", in *Proc. Int. conf. on Power Electronics and Drive systems (PEDS)*, pp. 491-496, Nov. 2003.

[29] H. N. Phyu, "Numerical Analysis of Brushless Permanent Magnet DC Motor using Couple Systems," PhD Thesis, *Department of Electrical and Computer Engineering, National University of Singapore*, 2004.

[30] S. L. Ho, H. L. Li, W. N. Fu, and H. C. Wong, "A Novel Approach to Circuit-Field-Torque Coupled Time Stepping Finite Element Modeling of Electric Machines," *IEEE Tran. Magn.*, vol. 36, no. 4, pp. 1886 - 1889, Jul. 2000.

[31] J. R. Brauer, *What every Engineer should know about Finite element method*, New York: Marcel Dekker, 1993.

[32] P. P. Silvester and R. L. Ferrari, *Finite Elements for Electrical Engineers*, 3rd ed, Great Britain: Cambridge University Press, 1996.

[33] Y. Duan, and D. M. Ionel, "A Review of Recent Developments in Electrical Machine Design Optimization Methods with a Permanent-Magnet Synchronous Motor Benchmark Study," *IEEE Trans. Ind. Appl.*, vol. 49, no. 3, May-Jun. 2013.

[34] M. A. Jabbar, Z. Liu and J. Dong, " Time-Stepping Finite-Element Analysis for the Dynamic Performance of a Permanent Magnet Synchronous Motor," *IEEE Trans. Magn.* , vol. 39, no. 5, Sep. 2003.

[35] C. Boccaletti, S. Elia, and E. Nisticò, "Deterministic and Stochastic Optimisation Algorithms in Conventional Design of Axial Flux PM Machines," in *Proc. Int. Symposium on Power Electronics, Electrical Drives, Automation and Motion*, pp. 111-115, May 2006.

[36] B. N. Cassimere and S. D. Sudhoff, "Population-based Design of Surface Mounted Permanent-Magnet Synchronous Machines," *IEEE Trans. Energy Convers.*, vol. 24, no. 2, pp. 338–346, Jun. 2009.

[37] S. Sonoda, Y. Takahashi, K. Kawagishi, N. Nishida, and S. Wakao, "Application of Stepwise Multiple Regression to Design Optimization of Electric Machine," *IEEE Trans. Magn.,* vol. 43, no. 4, pp. 1609–1612, Apr. 2007.

[38] L. Jolly, M. Jabbar, and L. Qinghua, "Design Optimization of Permanent Magnet Motors using Response Surface Methodology and Genetic Algorithms," *IEEE Trans. Magn.,* vol. 41, no. 10, pp. 3928–3930, Oct. 2005.

[39] N. Boules, "Design Optimization of Permanent Magnet DC Motors," *IEEE Trans. Ind. Appl.,* vol. 26, no. 4, pp. 786–792, Jul.-Aug. 1990.

[40] J. Legranger, G. Friedrich, S. Vivier, and J. C. Mipo, "Combination of Finite-Element and Analytical Models in the Optimal Multidomain Design of Machines: Application to an Interior Permanent-Magnet Starter Generator," *IEEE Trans. Ind. Appl.,* vol. 46, no. 1, pp. 232–239, Jan.-Feb. 2010.

[41] S. Kwon, S. Park, and J. Lee, "Optimum Design Criteria based on the rated watt of a Synchronous Reluctance Motor using a Coupled FEM and SUMT," *IEEE Trans. Magn.,* vol. 41, no. 10, pp. 3970–3972, Oct. 2005.

[42] S. J. Mun, Y. H. Cho, and J. H. Lee, "Optimum Design of Synchronous Reluctance Motors based on Torque/Volume using Finite-Element Method and Sequential Unconstrained Minimization Technique," *IEEE Trans. Magn.,* vol. 44, no. 11, pp. 4143–4146, Nov. 2008.

[43] D. Kocabas, "Novel Winding and Core Design for Maximum Reduction of Harmonic Magnetomotive Force in AC Motors," *IEEE Trans. Magn.,* vol. 45, no. 2, pp. 735–746, Feb. 2009.

[44] L. Chedot, G. Friedrich, J.M. Biedinger, and P. Macret, “Integrated Starter Generator: The need for an Optimal Design and Control Approach. Application to a Permanent Magnet Machine,” *IEEE Trans. Ind. Appl.*, vol. 43, no. 2, pp. 551–559, Mar.-Apr. 2007.

[45] H. Lee, and M. Noh, “Optimal Design of Radial-Flux Toroidally Wound Brushless DC Machines,” *IEEE Trans. Ind. Electron*, vol. 58, no. 2, pp. 444–449, Feb. 2011.

[46] X. Jannot, J. C. Vannier , C. Marchand, M. Gabsi, J. Saint-Michel and D. Sadarnac, “ Multiphysic Modeling of a High-Speed Interior Permanent-Magnet Synchronous Machine for a Multiobjective Optimal Design,” *IEEE Trans. Energy Convers.*, vol. 26, no. 2, pp. 457-467, Jun. 2011.

[47] D. K. Lim, and H. K. Jung, “Shape Optimization for Interior Permanent Magnet Motor Based on Hybrid Optimization Algorithm,” in *Proc. Electromagnetic Field Problems and Appli. (ICEF*), pp. 1-4, Jun. 2012.

[48] B. Kim, K. Y. Hwang, and B. I. Kwon, “ Optimization of Two-Phase In-Wheel IPMSM for Wide Speed Range by Using the Kriging Model Based on Latin Hypercube Sampling,” *IEEE Trans. Magn.*, vol. 47, no. 5, pp. 1078 – 1081, May 2011.

[49] Y. L. Karnavas, C. D. Korkas, “Optimization Methods Evaluation for the Design of Radial Flux Surface PMSM,” in *Proc. Int. Conf. Electrical Machines (ICEM)*, pp. 1348 – 1355, Sept. 2014.

[50] X. Jannot , J. C. Vannier , C. Marchand, M. Gabsi, J. Saint-Michel and D. Sadarnac, “ Multiphysics Modeling of a High-Speed Interior Permanent-Magnet Synchronous Machine for a Multi-objective Optimal Design,” *IEEE Trans. Energy Convers.*, vol. 26, no. 2, pp. 457-467, Jun. 2011.

[51] T. Hamiti, C. Gerada, and M. Rottach, “Weight Optimisation of a Surface Mount Permanent Magnet Synchronous Motor using Genetic Algorithms and a Combined Electromagnetic-Thermal Co-Simulation Environment,” in *Proc. Energy Conversion Congress and Exposition (ECCE)*, pp. 1536 – 1540, Sept. 2011.

[52] L. Liu, D. A. Cartes and W. Liu, “Particle Swarm Optimization Based Parameter Identification Applied to PMSM,” *American Control Conf.*, pp. 1-4, Jul. 2007.

[53] L. Liu, D.A. Cartes, and W. Liu, “Application of Particle Swarm Optimization to PMSM Stator Fault Diagnosis,” *Int. Joint Conf. on Neural Networks*, Jul. 2006.

[54] Y. Duan, and R. G. Harley, “A Novel Method for Multi-Objective Design and Optimization of Three Phase Induction Machines,” in *Proc. Energy Conv. Congress and Exposition (ECCE)*, pp: 284 – 291, Sept. 2010.

[55] X. Liu, H. Chen, J. Zhao, and A. Belahcen, “Research on the Performances and Parameters of Interior PMSM Used for Electric Vehicles,” *IEEE Trans. Ind. Electron.*, vol. 63, no. 6, pp. 3533-3545, Jun. 2016.

[56] K.I. Laskaris, and A.G.Kladas, “Internal Permanent Magnet Motor Design for Electric Vehicle Drive,” *IEEE Trans. Ind. Electron.*, vol. 57, no 1, pp. 138–145, Jan. 2010.

[57] K.T. Chau, C.C. Chan, and C. Liu, “Overview of Permanent-Magnet Brushless Drive for Electric and Hybrid Electric Vehicles,” *IEEE Trans. Ind. Electron.*, vol. 55, no. 6, pp. 2246–2257, Jun. 2008.

[58] F. Libert, “Design, Optimization and Comparison of Permanent Magnet Motors for a Low-Speed Direct-Driven Mixer,” Ph.D. thesis, *Royal Institute of Technology, Department of Electrical Engineering*, Nov. 2004.

[59] N. Korn, T. Vaimann, A. Kallaste, and A. Belahcen, “Comparative study of slow-speed slotless synchronous generator using SmCo and NdFeB permanent magnets,” in *Proc. Electric Power Quality and Supply Reliability Conf. (PQ)*, pp. 247-250, Jun. 2014.

[60] H. Hua, Z.Q. Zhu, M. Zheng, Z.Z. Wu, D. Wu, and X. Ge, “Performance Comparison of Partitioned Stator Machines with NdFeB and Ferrite Magnets,” in *Proc. IEEE Int. Electric Machines & Drives Conf. (IEMDC)*, pp. 461-467, May. 2015.

[61] Sintered NdFeB Magnets [Online], Available: http://www.mmcmagnetics.com

[62] P. Thelin, “Design and Evaluation of a Compact 15 Kw PM Integral Motor,” Ph.D thesis, *Royal Institute of Technology, Department of Electrical Engineering*, Feb. 2002.

[63] S.R P´erez, “Analysis of a Light Permanent Magnet in-wheel Motor for an Electric Vehicle with Autonomous Corner Modules,” MSc. thesis in Electrical Machines and Drives, *Royal Institute of Technology, School of Electrical engineering*, Feb. 2011.

[64] A. E. Fitzgerald, C. Kingsley, Jr., S. D. Umans, *Electric machinery*, 6th ed., New York: *Mc Graw Hill*, 2003, pp. 1-40

[65] Product Data Bulletin Selection of Electrical Steels for Magnetic Cores [Online], Available: www.aksteel.com.

[66] T. A. Lipo, *Introduction to AC Machine Design*, 3rd ed., Wisconsin power electronics research center, University of Wisconsin, pp. 281-287, 2011.

[67] J. H. Prudell, “Novel Design and Implementation of a Permanent Magnet Linear Tubular Generator for Ocean Wave Energy Conversion,” MSc. thesis in Electrical and Computer Engineering, *Oregon State University*, Dec. 2007.

[68] M. Iorgulescu, “Study of Single Phase Induction Motor with Aluminium versus Copper Stator Winding,” in *Proc. Int. Conf. on Applied and Theoretical Electricity (ICATE)*, pp. 1-5, Oct. 2016.

[69] Properties Table of Stainless Steel, Metals and other Conductive Materials [Online], Available: www.tibtech.com.

[70] Power Transmission/Linear Motion/Shafts [Online], Available: www.mcmaster.com.

[71] AST Bearings and Related Products & Services [Online], Available: www.astbearings.com/pillow-blocks-flanges.com

[72] A. M. EL-Refaie, Z. Q. Zhu, T. M. Jahns, and D. Howe, “Winding Inductances of Fractional Slot Surface Mounted Permanent Magnet Brushless Machines,” in *Proc. Ind. Appli. Society Annual Meeting (IAS)*, pp 1-8, Oct. 2008.

[73] C. Yu, R. Qu, W. Xu, and J. Li, “Analytical Determination of Optimal Split Ratio for Interior Permanent Magnet Synchronous Motor,” in *Proc. IEEE Transp. Electrification. Conf. (ITEC Asia-Pacific)*, pp. 1-5, Aug. 2014.

[74] Y. Pang, Z. Q. Zhu, and D. Howe, “Analytical Determination of the Optimal Split Ratio for Permanent Magnet Brushless Motors,” *IET Electric Power Appl.*, vol. 153, no. 1, pp. 7-13, Feb. 2006.

[75] Q. Li, M. Dou, and C. Fang, “Analytical Determination of Optimal Split Ratio for High Speed Permanent Magnet Brushless Motors,” in *Proc. Int. Conf. Electrical Machines and Systems (ICEMS)*, pp. 636-640, Oct. 2015.

[76] T. Heikkila, “Permanent Magnet Synchronous Motor for Industrial Inverter Applications - Analysis and Design,” Ph.D. thesis, *Lappeenranta University of Technology*, Nov. 2002.

[77] Y. Duan, R. G. Harley and T. G. Habetler, “Comparison of Particle Swarm Optimization and Genetic Algorithm in the Design of Permanent Magnet Motors,” in *Proc. Power Electronics and Motion Control Conf. (IPEMC)*, pp. 822 – 825, May 2009.

[78] D. Whitley, “A Genetic Algorithm tutorial,” *Statistics and Computing*, vol. 4, pp. 65–85, Jan. 1994.

[79] L. Hamm, B. W. Brorsen, and M. T. Hagan, “Comparison of Stochastic Global Optimization Methods to Estimate Neural NetworkWeights,” *Neural Processing Letters*, vol. 26, issue 3, pp. 145–158, Dec. 2007.

[80] R. A. Krohling, E. Mendel, M. Campos, “Swarm algorithms with chaotic jumps for optimization of multi-modal functions,” *Engineering Optimization*, vol. 43, no. 11, pp. 1243–1261, Mar. 2011.

[81] S. N. Sivanandam, and S. N. Deepa, *Introduction to Genetic Algorithms*, New York: Springer Berlin Heidelberg, pp. 15-36, 2008.

[82] G.J Park, D. Lee, J.W. Kim, and S. Y. Jung, “Intelligent Simplex Method for Optimal Design of Electric Machine,” in *Proc. IET Int. Conf. on Computation in Electromagnetics* ,pp.1-2, Apr. 2014.

[83] W. Press, S. Teukolsky, W. Vetterling and B. Flannery, *Numerical Recipes in Fortran 77*, New York: Cambridge University press, pp. 402-406, 1997.

[84] K. Kobravi, and S. Filizadeh, "*An Adaptive Multi-Modal Optimization Algorithm for Simulation-Based Design of Power-Electronic Circuits,*" Engineering Optimization, vol. 41, no. 10, pp. 945–969, Oct. 2009.

[85] F. Yahyaie, S. Filizadeh, "A Surrogate-Model Based Multi-Modal Optimization Algorithm," *Engineering Optimization*, vol. 43, no. 7, pp. 779–799, July 2011.

[86] A. Y. Goharrizi, R. Singh, A. M. Gole, S. Filizadeh, J. C. Muller, R. Jayasinghe, "A Parallel Multi-Modal Optimization Algorithm for Simulation-Based Design of Power Systems," *IEEE Trans. Power Del.*, vol. 30, no. 5, pp. 2128-2137, Oct. 2015.

[87] M. C. Fu, "Optimization via Simulation: A Review," *Ann. Oper. Res.*, vol. 53, no. 8, pp. 199–248, 1994.

[88] A. Ravindran, K. M. Ragsdell, G. V. Reklaitis, *Engineering Optimization: Methods and Applications*, 2nd ed., New Jersey: John Wiley & Sons, 2006.

[89] S. Stipetic, W. Miebach, and D. Zarko "Optimization in design of electric machines: Methodology and workflow," in *Proc. joint conf. Electrical Machines & Power Electronics (ACEMP), 2015 Intl Conf. on Optimization of Electrical & Electronic Equipment (OPTIM) & 2015 Intl Symposium on Advanced Electromechanical Motion Systems (ELECTROMOTION)*, pp. 441-448, Sept. 2015.

[90] S. Meier, "Theoretical design of Surface-Mounted Permanent Magnet motors with Field Weakening Capability," MSc. thesis, *Royal Institute of Technology*, Mar. 2002.

[91] A. M. EL-Refaie, M. R. Shah, J. P. Alexander , S. Galioto, Kum-Kang Huh and W. D. Gerstler, "Rotor End Losses in Multiphase Fractional-Slot Concentrated-Winding Permanent Magnet Synchronous Machines," *IEEE Trans. Ind. Appl.*, vol. 47, no. 5, pp. 2066-2074, Sept.-Oct. 2011.

[92] S. R. P´erez, "Analysis of a Light Permanent Magnet In-Wheel Motor for an Electric Vehicle with Autonomous Corner Modules," MSc. thesis, *Royal Institute of Technology, School of Electrical engineering*, Feb. 2011.

[93] M. S. Toulabi, "Wide Speed Range Operation of Concentrated Winding Interior Permanent Magnet Synchronous Machines," Ph.D. thesis, *University of Alberta*, 2016.